Spectroscopic Characterization of the Catalytically Competent Ferrous Site of the Resting, Activated, and Substrate-Bound Forms of Phenylalanine Hydroxylase

Kelly E. Loeb,[†] Tami E. Westre,[†] T. Joseph Kappock,[‡] Nataša Mitić,[‡] Elizabeth Glasfeld,[‡] John P. Caradonna,*[,‡] Britt Hedman,*[,§] Keith O. Hodgson,*[,†,§] and Edward I. Solomon*[,†]

Contribution from the Department of Chemistry and Stanford Synchrotron Radiation Laboratory, Stanford University, Stanford, California 94305, and Department of Chemistry, Yale University, New Haven, Connecticut 06520

Received July 3, 1996[⊗]

Abstract: The geometric structure of the catalytically relevant ferrous active site of phenylalanine hydroxylase (PAH) has been investigated using magnetic circular dichroism (MCD) and X-ray absorption (XAS) spectroscopies. From the excited state ligand field transitions in the MCD spectrum ($10Dq = 9400$ cm^{-1}, $\Delta^5E_g = 1800$ cm^{-1}), the temperature and field dependence of these transitions ($\Delta^5T_{2g} = 590$ cm^{-1}), and the XAS pre-edge shapes and intensities, the resting ferrous site of the "tense" form of PAH is six-coordinate distorted octahedral. The low ligand field strength observed in the MCD spectrum results from significant oxygen ligation and longer Fe−O/N bond distances relative to model complexes as determined from an EXAFS analysis. Nonallosteric activation using *N*-ethylmaleimide does not notably affect the band positions in the MCD spectrum and therefore does not perturb the structure of the iron center. However, substrate addition without allosteric activation results in a different six-coordinate distorted octahedral structure as determined by MCD ($10Dq = 10\,000$ cm^{-1}, $\Delta^5E_g = 1450$ cm^{-1}) and XAS with a greater d_π-orbital splitting ($\Delta^5T_{2g} = 1050$ cm^{-1}). EXAFS analysis indicates a shift in the relative number of ligands from the outer to the inner subshell of the first coordination sphere in the substrate-bound form of the enzyme relative to the resting site, consistent with the increased ligand field strength observed directly from the MCD spectrum. Substrate-induced allosteric activation (∼34 kcal/mol) does not alter the structure of the iron site in the "relaxed" form of PAH compared to the substrate-bound "tense" state. Thus, while activation is necessary for the enzyme to achieve complete catalytic competence, it does not appear to affect the geometry of the catalytically relevant six-coordinate ferrous active site and only directly influences the surrounding protein conformation. In contrast, substrate addition results in a geometric and electronic structural change at the iron center which may help orient the substrate for completely coupled hydroxylation.

Introduction

Mononuclear non-heme iron-containing enzymes perform a variety of important catalytic functions requiring the binding and activation of dioxygen. This diverse group of systems can be divided into classes according to the types of reactions that are catalyzed: monooxygenation (pterin-dependent hydroxylases[1,2] and ω-hydroxylase[3]), dismutation (superoxide dismutase[4]), oxidation (isopenicillin N synthase[5]), hydroperoxidation (soybean lipoxygenase[6]), and dioxygenation. The dioxygenases can be further broken down into subclasses: extra- (catechol 2,3-dioxygenase) and intradiol (protocatechuate 3,4-dioxygenase) dioxygenases,[7,8] *cis*-dihydroxylases (phthalate dioxygenase[9]), and α-ketoglutarate-dependent hydroxylases (clavaminate synthase[10]).

The class of tetrahydropterin (PH_4)-dependent hydroxylases,[2] which consists of phenylalanine[11] (PAH), tyrosine[12−14] (TyrH), and tryptophan[15,16] (TrpH) hydroxylases, performs several important functions in biological chemistry, including activation of O_2 for highly specific oxidation reactions, regulation of aromatic amino acid metabolism, and mediation for the health and proper functioning of the brain. PAH initiates the detoxification of high levels of phenylalanine, and its deficiency from the liver and kidney leads to the genetic disorder phenylketonuria (PKU).[17−19] This condition affects one in 10 000 infants in the

[†] Department of Chemistry, Stanford University.
[‡] Department of Chemistry, Yale University.
[§] Stanford Synchrotron Radiation Laboratory.
[⊗] Abstract published in *Advance ACS Abstracts,* February 1, 1997.

(1) Shiman, R. In *Folates and Pterins: Chemistry and Biochemistry of Pterins*; Blakley, R. L., Benkovic, S. J., Eds.; John Wiley & Sons: New York, 1985; Vol. 2, p 179.
(2) Kappock, T. J.; Caradonna, J. P. *Chem. Rev.* **1996**, *96*, 2659.
(3) Katopodis, A. G.; Wimalasena, K.; Lee, J.; May, S. W. *J. Am. Chem. Soc.* **1984**, *106*, 7928.
(4) Stoddard, B. L.; Howell, P. L.; Ringe, D.; Petsko, G. A. *Biochemistry* **1990**, *29*, 8885.
(5) Baldwin, J. E.; Bradley, M. *Chem. Rev.* **1990**, *90*, 1079.
(6) Samuelsson, B.; Dahlén, S.-E.; Lindgren, J. Å.; Rouzer, C. A.; Serhan, C. N. *Science* **1987**, *237*, 1171.
(7) Que, L., Jr. In *Iron Carriers and Iron Proteins*; Loehr, T. M., Ed.; VCH Publishers, Inc.: New York, 1989; Vol. 5, p 467.
(8) Lipscomb, J. D.; Orville, A. M. In *Metal Ions in Biological Systems*; Sigel, H., Sigel, A., Eds.; Marcel Dekker, Inc.: New York, 1992; Vol. 28, p 243.
(9) Batie, C. J.; LaHaie, E.; Ballou, D. P. *J. Biol. Chem.* **1987**, *262*, 1510.
(10) Salowe, S. P.; Marsh, E. N.; Townsend, C. A. *Biochemistry* **1990**, *29*, 6499.
(11) Kaufman, S. *Adv. Enzymol. Relat. Areas Mol. Biol.* **1993**, *67*, 77.
(12) Kaufman, S.; Kaufman, E. E. *Tyrosine Hydroxylase*; John Wiley & Sons: New York, 1985; Vol. 2.
(13) Dix, T. A.; Kuhn, D. M.; Benkovic, S. J. *Biochemistry* **1987**, *26*, 3354.
(14) Fitzpatrick, P. F. *Biochemistry* **1991**, *30*, 3658.
(15) Kuhn, D. M.; Ruskin, B.; Lovenberg, W. *J. Biol. Chem.* **1980**, *255*, 4137.
(16) Kuhn, D. M.; Lovenberg, W. In *Folates and Pterins: Chemistry and Biochemistry of Pterins*; Blakley, R. L., Benkovic, S. J., Eds.; John Wiley & Sons: New York, 1985; Vol. 2, p 353.

S0002-7863(96)02269-X CCC: $14.00

United States and is characterized by irreversible, progressive brain damage and severe mental retardation. TyrH catalyzes the formation of L-DOPA from L-tyrosine, which is the rate-limiting step in the biosynthesis of the catecholamine neurohormone dopamine and the neurotransmitters norepinephrine and epinephrine. Similarly, TrpH is involved in the rate-limiting step of serotonin biosynthesis but is the least well-understood of the three enzymes owing to difficulties in purification and its low activity, instability, and tissue concentration.

Rat hepatic PAH, which is the most extensively studied of the tetrahydrobiopterin (BH_4)-dependent hydroxylases due to its greater availability, soluble nature, and relative ease of purification by reversible substrate-induced hydrophobic binding, serves as the prototype aromatic amino acid hydroxylase.[1,2,11] All of the pterin-dependent hydroxylases are thought to contain similar active sites as a consequence of the very high conservation of residues in the catalytic domain, their common reduced pterin cofactor requirement, and similar substrates. PAH is a tetramer of 51.7 kDa subunits, each of which contains a non-heme iron required for reactivity.[20] During the hydroxylation of phenylalanine, the enzyme uses dioxygen and BH_4 to generate tyrosine and quinonoid dihydrobiopterin (q-BH_2) via a putative C4a-hydroperoxy dihydrobiopterin species in a tightly coupled fashion. Dioxygen is partitioned between the phenolic hydroxy group of tyrosine and the initial C4a-carbinolamine form of the oxidized pterin, which subsequently dehydrates to yield q-BH_2. In order to avoid depletion of phenylalanine, the enzyme is only active in the presence of elevated levels of its amino acid substrate, L-phenylalanine. Phenylalanine cooperatively binds to an allosteric effector site that is distinct from the catalytic site[21] and remains bound at this site during multiple catalytic cycles.[22] Using the Monod, Wyman, Changeux nomenclature,[23] this transition between the resting low-affinity ("tense") state (PAH^T) and the activated high-affinity ("relaxed") state (PAH^R) has a large energetic barrier (~34 kcal/mol) and is accompanied by a significant structural rearrangment of the protein.[22,24] Enzyme activation can also be accomplished using detergents (lysolecithin), proteases (α-chymotrypsin), or sulfhydryl modifying reagents (*N*-ethylmaleimide).[25] For the reaction of the resting enzyme with the natural BH_4, an ordered sequential mechanism is observed,[26] phenylalanine + BH_4 + O_2, because tight binding of the pterin to the resting enzyme inhibits its conversion to the activated state.[1,27]

A role for the non-heme iron in oxygen activation is strongly suggested since all of the mammalian hydroxylases contain one non-heme iron per subunit and each enzyme requires the presence of its metal center for reactivity.[13,15,20] It has been proposed that dioxygen reacts directly with the pterin cofactor to generate a 4a-hydroperoxytetrahydrobiopterin (4a-hydroperoxy = 4a-OOH), which then reacts further to form the active oxidant.[28,29] According to this mechanism, Fe(II) would react with the peroxidated cofactor, rather than with dioxygen itself, forming a μ-peroxypterin−iron complex (4a-OO-Fe). Heterolytic decomposition of this intermediate would further generate a non-heme oxo−ferryl intermediate that is the active oxidant and the observed 4a-hydroxypterin ((4a-OH)BH_2) species. Little direct evidence exists as to the nature of the iron coordination sphere, but it is proposed to lie in close proximity to the pterin binding domain possibly with direct cofactor binding[30] and consist of nitrogen and oxygen ligation from histidine and carboxylate residues, respectively, and possibly a water-based ligand.[31,32]

Prior to becoming catalytically competent, the ferric state of the enzyme must be reduced by BH_4; in the presence of all three of its substrates, PAH oxidizes once in every 150−200 catalytic turnovers under tightly coupled conditions.[28,33,34] It is therefore critically important to define the nature of the reduced resting site as a basis to further probe substrate- and cofactor-bound forms along the mechanistic pathway. However, most studies thus far reported on PAH have been on the resting ferric site which is electron paramagnetic resonance (EPR) active and thus more spectroscopically accessible.[33,35] We have employed two methodologies (magnetic circular dichroism[36] and X-ray absorption edge[37] spectroscopies) for the study of mononuclear non-heme ferrous systems.[38−43] Magnetic circular dichroism (MCD) spectroscopy in the near-infrared (near-IR) energy region allows one to directly observe ligand field d → d transitions. These excited state d_σ-orbital energies are sensitive to the coordination number and geometry at the iron active site. In addition, variable temperature variable field (VTVH) MCD spectroscopy can be used to extract the ground state sublevel splittings for these EPR inactive non-Kramers ions, which can then be related to the ground state d_π-orbital energies. Taken together, a complete experimentally determined d-orbital energy diagram is obtained. X-ray absorption edge spectroscopy (XAS) at the iron K-edge provides complementary information on the oxidation and spin states, coordination number, and geometry at the iron center. In particular, the number of peaks contributing to the 1s → 3d pre-edge feature and their relative intensity distribution depend on the available final states and are therefore sensitive to the oxidation and spin states of the iron. Further-

(17) Eisensmith, R. C.; Woo, S. L. C. *Adv. Genet.* **1995**, *32*, 199.
(18) Scriver, C. R.; Kaufman, S.; Eisensmith, R. C.; Woo, S. L. C. In *The Metabolic and Molecular Bases of Inherited Disease*, 7th ed.; Scriver, C. R., Beaudet, A. L., Sly, W. S., Valle, D., Eds.; McGraw-Hill: New York, 1995; Vol. 1.
(19) Scriver, C. R.; Eisensmith, R. C.; Woo, S. L. C.; Kaufman, S. *Annu. Rev. Genet.* **1994**, *28*, 141.
(20) Gottschall, D. W.; Dietrich, R. F.; Benkovic, S. J.; Shiman, R. *J. Biol. Chem.* **1982**, *257*, 845.
(21) Shiman, R. *J. Biol. Chem.* **1980**, *255*, 10029.
(22) Shiman, R.; Jones, S. H.; Gray, D. W. *J. Biol. Chem.* **1990**, *265*, 11633.
(23) Monod, J.; Wyman, J.; Changeux, J. *J. Mol. Biol.* **1965**, *12*, 88.
(24) Shiman, R.; Gray, D. W. *J. Biol. Chem.* **1980**, *255*, 4793.
(25) Fisher, D. B.; Kaufman, S. *J. Biol. Chem.* **1973**, *248*, 4345.
(26) Tourian, A. *Biochim. Biophys. Acta* **1971**, *242*, 345.
(27) Xia, T.; Gray, D. W.; Shiman, R. *J. Biol. Chem.* **1994**, *269*, 24657.
(28) Dix, T. A.; Benkovic, S. J. *Biochemistry* **1985**, *24*, 5839.
(29) Dix, T. A.; Bollag, G. E.; Domanico, P. L.; Benkovic, S. J. *Biochemistry* **1985**, *24*, 2955.
(30) Martínez, A.; Abeygunawardana, C.; Haavik, J.; Flatmark, T.; Mildvan, A. S. *Adv. Exp. Med. Biol.* **1993**, *338*, 77.
(31) Glasfeld, E.; Xia, Y.-M.; Debrunner, P. G.; Caradonna, J. P. Submitted for publication.
(32) Martínez, A.; Olafsdottir, S.; Flatmark, T. *Eur. J. Biochem.* **1993**, *211*, 259.
(33) Wallick, D. E.; Bloom, L. M.; Gaffney, B. J.; Benkovic, S. J. *Biochemistry* **1984**, *23*, 1295.
(34) Shiman, R.; Gray, D. W.; Hill, M. A. *J. Biol. Chem.* **1994**, *269*, 24637.
(35) Bloom, L. M.; Benkovic, S. J.; Gaffney, B. J. *Biochemistry* **1986**, *25*, 4204.
(36) Solomon, E. I.; Pavel, E. G.; Loeb, K. E.; Campochiaro, C. *Coord. Chem. Rev.* **1995**, *144*, 369.
(37) Westre, T. E.; Kennepohl, P.; DeWitt, J. G.; Hedman, B.; Hodgson, K. O.; Solomon, E. I. Submitted for publication.
(38) Kasibhatla, B. T.; Loeb, K. E.; Westre, T. E.; Rodriguez, J. H.; Debrunner, P. G.; Hedman, B.; Hodgson, K. O.; Solomon, E. I.; Caradonna, J. P. Manuscript in preparation.
(39) Loeb, K. E.; Zaleski, J. M.; Westre, T. E.; Guajardo, R. J.; Mascharak, P. K.; Hedman, B.; Hodgson, K. O.; Solomon, E. I. *J. Am. Chem. Soc.* **1995**, *117*, 4545.
(40) Pavlosky, M. A.; Zhang, Y.; Westre, T. E.; Gan, Q.-F.; Pavel, E. G.; Campochiaro, C.; Hedman, B.; Hodgson, K. O.; Solomon, E. I. *J. Am. Chem. Soc.* **1995**, *117*, 4316.
(41) Pavel, E. G.; Martins, L. J.; Ellis, W. R., Jr.; Solomon, E. I. *Chem. Biol.* **1994**, *1*, 173.
(42) Mabrouk, P. A.; Orville, A. M.; Lipscomb, J. D.; Solomon, E. I. *J. Am. Chem. Soc.* **1991**, *113*, 4053.
(43) Whittaker, J. W.; Solomon, E. I. *J. Am. Chem. Soc.* **1988**, *110*, 5329.

more, information about the types of ligands and the ligand distances can be obtained by analysis of the extended X-ray absorption fine structure (EXAFS) region of the XAS spectrum. These MCD and XAS techniques, which individually provide information on the geometric and electronic structure of the ferrous center, combine to furnish insight into oxygen binding and activation at these important mononuclear non-heme iron active sites.

We have applied the above protocols to {Fe^{2+}}PAH to probe spectroscopically the catalytically relevant ferrous oxidation state and various substrate-bound forms related to the enzyme mechanism. Initially, a series of {Fe^{2+}}PAH samples was studied to explore different possible chemical perturbations including substrate (L-phenylalanine) and substrate analog (L-tryptophan) binding, and allosteric (L-phenylalanine + ∼34 kcal/mol) and alternative methods (*N*-ethylmaleimide, NEM) of activation. Excited state MCD was able to differentiate two forms of {Fe^{2+}}PAH, one free of L-phenylalanine at the catalytic site (denoted PAH[ ]) and the other with L-phenylalanine present at this site (denoted PAH[L-phe]), each of which was insensitive to the level of activation of the enzyme. More detailed spectroscopy was pursued on these two structures employing both VTVH MCD and XAS in an effort to understand specific changes induced at the iron center by the presence of the natural phenylalanine substrate. Finally, XAS studies were extended to the ferric counterparts of these species to determine if similar trends are observed in this noncatalytic oxidation state which requires reduction by its cofactor to achieve complete catalytic competence.

Experimental Section

PAH Isolation. All commercial reagents were of the highest grade available and were used without further purification, with the exception of glycerol, which was treated with activated carbon to remove contaminants as previously described.[44] Glycerol, L-phenylalanine, L-tryptophan, hemisodium MOPS, and other supplies were from Sigma (St. Louis, MO). Sodium dithionite and D_2O (99.9 atom % D) were from Aldrich (Milwaukee, WI), and potassium chloride was from Mallinckrodt (Paris, KY). Glycerol-d_3 (98 atom % D) was from Cambridge Isotopes Laboratories (Andover, MA).

Recombinant rat liver PAH was overexpressed in *Escherichia coli* and purified using a variation of the hydrophobic affinity method[44] as previously described.[45] PAH purified from this source is unphosphorylated, highly active, and derived from a single (W) allele, all of which remove potential sources of sample inhomogeneity. Furthermore, the overexpression of PAH allows the isolation of protein containing catalytically competent bound iron (∼98%), thereby avoiding problems associated with deconvoluting the spectroscopic features of active iron from adventitiously-bound iron. EPR spectroscopy shows a correspondingly small purely rhombic contribution from "inactive iron" species (∼2%).[46] Purified PAH was stored at −70 °C and thawed immediately before use. The specific activities of PAH samples used in the current work were all ≥6.0 units mg^{-1}, where 1 unit = 1 μmol of L-tyrosine min^{-1}. For enzyme having ∼0.6 Fe subunit^{-1} this corresponds to a specific activity of 10 units mg^{-1} for fully loaded enzyme, which compares well with the highest reported literature value of 14 units mg^{-1}.[1,2] Since freeze−thaw cycles reduce the activity of PAH,[44] specific activities, iron content, and electrophoretic homogeneity were determined for each enzyme purification using parallel samples reserved for these purposes.

All protein manipulations required for the preparation of specific PAH sample states for spectroscopic analysis were performed at 4 °C. Buffers and solutions for those samples requiring anaerobic conditions were thoroughly degassed using three freeze−pump−thaw cycles. The glycerol-containing solutions were stored under dry N_2, and their exposure to air was minimized. Typically ≥20−25 mg of protein was used in the preparation of each sample.

Preparation of PAH^T Sample for MCD. The PAH^T samples were diluted to approximately 1 mg mL^{-1} in phenylalanine-free buffer (0.1 M MOPS, 0.3 M KCl; pH 7.3 at 25 °C). The dilute protein solution was filtered through a 0.45 μm syringe filter to remove aggregates and then concentrated in a 50 mL Amicon ultrafiltration device over a YM30 membrane (45 mm) using pressurized N_2 to a final volume of ∼1 mL. This concentrated sample was then placed in an Eppendorf tube and centrifuged at 14 000 rpm for 2 min to remove any precipitated protein. The protein sample was exchanged five times into 0.1 M MOPS, 0.3 M KCl buffer made up in D_2O and adjusted to a pD ∼ 7.3 (pH ∼ 6.9) with DCl. In each exchange, the protein solution was concentrated to ≤1 mL and 5 mL of deuterated buffer was added, except in the final exchange, when it was concentrated down to 200 μL. The PAH solution was spun in between the D_2O exchanges to remove aggregates and prevent further precipitation. The final aqueous protein concentration was determined by the Bradford dye binding assay as previously described.[45] An aliquot of this sample (without glycerol-d_3) was set aside for room temperature circular dichroism (CD) experiments. To facilitate glass formation for the low-temperature MCD experiments, the concentrated aqueous protein solution was diluted with several volumes of 60−75% glycerol-d_3 in deuterated buffer. In order to ensure complete mixing, the glycerol-d_3 was added slowly with careful manual mixing, until a brief spin did not induce phase separation of the two components. The resulting ≥50% glycerol-d_3/PAH solution was concentrated to a final volume of 200−300 μL in a 3 mL Amicon ultrafiltration device over a YM30 membrane (25 mm). This process was very slow due to the high viscosity of the solution. Periodically during ultrafiltration, the N_2 pressure was slowly released and the protein concentration was determined in a diluted sample aliquot by the Bradford assay. Once a sample of the desired concentration was obtained, the entire ultrafiltration apparatus was placed in an Ar-filled glovebox, and strict anaerobic procedures were used for the remainder of the sample preparation. The protein sample (with or without glycerol-d_3) was reduced using a solution of sodium dithionite (in D_2O or 50% glycerol-d_3/D_2O) freshly standardized vs $K_3Fe(CN)_6$ (ferricyanide → ferrocyanide $\Delta\epsilon_{420nm} = 1020\ M^{-1}\ cm^{-1}$).[47] Sufficient dithionite to reduce protein-bound Fe(III) was added, causing an immediate bleaching of the characteristic yellow color of {Fe^{3+}}PAH (which is particularly prominent in glycerol). The reduced sample was stored in liquid N_2. For room temperature CD, the sample was thawed under a N_2 atmosphere, injected into a 1 cm path length near-IR cuvette, and sealed with a Kontes stopcock to prevent air oxidation during the time course of the experiment. The similarly thawed MCD sample was injected into a cell assembled under N_2 with a neoprene spacer (3 mm path length, 6 mm i.d., 12 mm o.d.) sandwiched between two Infrasil quartz disks and stabilized between two fitted copper plates. The sample was maintained under anaerobic conditions until insertion into the cryostat under a flow of He gas.

Preparation of PAH^R[L-phe] and PAH^R-NEM Samples for MCD. The PAH^R[L-phe] sample was prepared almost identically, except that the 1 mg mL^{-1} sample of protein was made 1.0 mM in L-phenylalanine using a 20 mM stock solution, incubated 10 min at 25 °C, and then filtered prior to the first concentration step. These conditions were sufficient to induce the allosteric activation process, which is necessary for the generation of a catalytically competent form of the enzyme.[44] Before the D_2O buffer exchange, more L-phenylalanine was added to bring the final concentration to 10 mM. All other manipulations were the same as those above except that 10 mM [L-phe] was present in all solutions. PAH^R-NEM is irreversibly activated by alkylation of Cys236. This alkylation was performed by incubating 28 mg of {Fe^{3+}}PAH^T[ ] at 1 mg mL^{-1} (20 μM [subunit]) with 25 μM *N*-ethylmaleimide for 45 min at 25 °C prior to filtration and the first concentration step. All subsequent manipulations were performed as described for the PAH^T sample.

Preparation of PAH^T[L-trp] and PAH^T[L-phe] Samples for MCD. The preparation of PAH^T[L-trp] samples was identical to the preparation of the PAH^T sample except that L-tryptophan was added to all solutions

(44) Shiman, R.; Gray, D. W.; Pater, A. *J. Biol. Chem.* **1979**, *254*, 11300.
(45) Kappock, T. J.; Harkins, P. C.; Friedenberg, S.; Caradonna, J. P. *J. Biol. Chem.* **1995**, *270*, 30532.
(46) Glasfeld, E. Ph.D. Thesis, Yale University, 1994.
(47) Williams, C. H., Jr.; Kamin, H. *J. Biol. Chem.* **1962**, *237*, 587.

Table 1. Protein Specifications for {Fe^{2+}}PAH CD and MCD Samples

enzyme state	init sp act. (units mg^{-1})	protein [ ] (mg mL^{-1})	% glycerol-d_3	[Fe(II)] (mM)	final sp act. (units mg^{-1})
{Fe^{2+}}PAH^T[ ]	6.9	105	50	1.3	6.1 (88%)[a]
{Fe^{2+}}PAH^R[L-phe]	6.8	122	72	2.0	5.8 (85%)
{Fe^{2+}}PAH^R-NEM	6.8	92	55	1.2	5.8 (85%)
{Fe^{2+}}PAH^T[L-phe]	6.8	100	50	1.3	6.0 (88%)
{Fe^{2+}}PAH^T[L-trp]	6.8	140	63	2.2	6.5 (95%)

[a] Percent of initial specific activity.

to maintain a final concentration of 8.3 mM. This concentration of L-tryptophan was insufficient to induce allosteric activation of the enzyme.[21,46] The PAH^T[L-trp] sample was also prepared like the PAH^R-[L-phe] sample, excluding the incubation at 25 °C and maintaining [L-trp] at 8.3 mM. The preparation of the PAH^T[L-phe] sample was identical to the PAH^T sample preparation, up to and including the dithionite reduction step. In order to prevent allosteric activation,[24] the sample was chilled in an ice/water slush in the inert atmosphere box and every precaution against heating the sample was employed. In one quick manipulation, the PAH sample was mixed with L-phenylalanine, loaded in a chilled syringe, immediately injected into a chilled MCD cell, and frozen in liquid N_2. The final concentration of L-phenylalanine was 1.0 mM, which would be sufficient to activate the enzyme were the sample warmed to 25 °C for 15 min. However, the rate at which the enzyme is activated by L-phe is expected to be relatively slow (25 °C, 1 mM L-phe) with a pseudo-first-order activation rate constant of 0.9 min^{-1} vs the catalytic rate under equivalent conditions (700 mol of Tyr formed per mol of subunit per minute).[1,2] Furthermore, the rate constant for activation shows a strong temperature dependence with an Arrhenius activation energy of approximately 35 kcal/mol, suggesting that any conversion of the PAH^T[L-phe] state to PAH^R[L-phe] at 4 °C is negligible during the short time (15 s) needed to perform the sample transfer.[1,2]

Verification of the assignment of the PAH^T[L-phe] state of the sample is based on four independent methods of assessment, (i) the steady-state kinetic properties, (ii) gel filtration experiments, (iii) EPR spectroscopy, and (iv) small-angle solution X-ray scattering studies. The steady-state kinetic studies of PAH show that PAH^T has less than 1% of the activity of PAH^R[L-phe].[1] The standard continuous enzyme assay used in this study to measure PAH activity is based on direct detection of tyrosine formation at 275 nm ($\epsilon_M = 17000$).[1,20,46] This method is sensitive, allowing the detection of catalytically competent enzyme at concentration levels 50-fold less than the enzyme concentrations used in our analyses. The absence of any observed activity for the PAH^T[L-phe] sample assayed under these conditions therefore places an upper bound of $\leq$2% for any activated PAH^R[L-phe] contamination. The second line of evidence supporting the assignment of the PAH^T-[L-phe] state arises from measurement of the Stokes radius of the protein.[45,48] Small-zone gel filtration experiments were performed by FPLC using a prepacked Superdex 200 26/60 analytical column (Pharmacia) in order to determine the peak retention times. Particular care was taken to assure reproducible starting times, an effort rewarded by highly reproducible retention times. In a typical experiment, 0.2−1 mg of protein was injected onto the column previously equilibrated at 4 °C in 0.1 M phosphate, pH 6.8 buffer, and eluted at 2.5 mL min^{-1} (28 cm h^{-1}) with detection at 280 nm. Molecular weights were determined by measuring the retention time of seven protein standards run under these conditions and converting the retention times to K_{av} values, where $K_{av} = (V_e - V_0)/(V_t - V_0)$ and V_0 is the void volume, determined from the retention time of Blue Dextran ($M \sim 2 \times 10^6$ Da), V_e is the elution volume of the peak of interest, and V_t is the included volume, determined from the retention time of acetone ($M =$ 58 Da). A plot of K_{av} vs log(M) is linear over the range of interest and was used to construct a standard curve. A calculation of the Stokes radius (RH) was made using the method of Siegel and Monty, in which the column is calibrated by plotting $(-\log K_{av})^{1/2}$ vs known RH values for several globular proteins (thyroglobulin, apoferritin, catalase, ADH (tetramer), BSA, ADH (dimer), and carbonic anhydrase).[49] Globular size standards (Sigma) used for determining the molecular weight and RH values are as previously published.[49] Experiments peformed on PAH^T[L-phe] included 1.0 mM L-phe in the buffer to prevent loss of L-phe from the active site.[48] PAH^T[ ] gave a K_{av} of 0.248 ± 0.001 (M = 248 ± 1 kDa) while the corresponding values for PAH^T[L-phe] and PAH^R[L-phe] were 0.244 (254 kDa) and 0.232 (272 kDa), respectively. This corresponds to Stokes radii of 55 Å for PAH^T[L-phe] and 57 Å for PAH^R[L-phe]. Thus, the Stokes radius of PAH^T[L-phe] resembles that of the T-state enzyme rather than the activated R-state form. No evidence of equilibration between these states was observed over the time course of these experiments. These data are also consistent with small-angle solution X-ray scattering studies (R_G (Å): PAH^T[L-phe] = 37.9 ± 0.2; PAH^R[L-phe] = 39.6 ± 0.2).[48,50] Confirmation that L-phe remains bound in the active site arises from the EPR spectra of ferric PAH in its different states.[46] The EPR spectrum of PAH^T[ ] is quite distinct from those of PAH^T[L-phe] and PAH^R[L-phe], which show the presence of a $g_{eff} = 4.5$ signal indicative of substrate binding in the active site. Equivalent spectra were also observed for PAH^T[L-trp]; L-trp cannot activate PAH under these conditions but can act as a substrate. In total, these data indicate that L-phe remains in the active site of PAH^T[L-phe] under these conditions and that its overall solution structure is equivalent to the resting PAH^T[ ] state. The lack of any detectable product formation indicates that the PAH^T[L-phe] is not catalytically competent, but can be converted to an active form only upon activation. The experimental results are therefore only consistent with the complete (≥95%) formation of the PAH^T[L-phe] state. It was observed during these studies that, owing to its hydrophobic nature, the allosteric activation of PAH at high concentrations induces immediate precipitation of the enzyme; no such precipitation was observed during the preparation of the PAH^T[L-phe] sample. Note that PAH activity measurements were performed on the MCD samples after spectroscopic analysis (Table 1) and all samples showed extremely high retention of enzymatic activity, indicating little sample degradation during the time course of the experimental measurements.

MCD Instrumentation. Room temperature near-IR CD spectra (278 K, 600−2000 nm) were obtained using a Jasco 200D spectropolarimeter interfaced to a Macintosh IIvx computer and a liquid N_2-cooled InSb detector. The sample temperatures were maintained by a recirculating water bath kept just below 278 K. Data acquisition was achieved using routines written within the software package LabVIEW (National Instruments). Contributions to the CD intensity due to buffer and cell backgrounds were subtracted from the raw protein CD spectra. Low-temperature near-IR MCD spectra (1.6−100 K, 600−2000 nm) were obtained with the Jasco 200D spectropolarimeter and an Oxford Instruments SM4000 7 tesla (T) superconducting magnet/cryostat. Depolarization of frozen samples (<10%) was measured by monitoring the CD intensity of a nickel (+)-tartrate solution placed equidistantly before and after the sample.[51] MCD spectra were corrected for zero-field base-line effects induced by cracks in the glasses by subtracting off the corresponding 0 T scan at each temperature. CD and MCD spectra were smoothed using a weighted fitting routine and resolved into Gaussian band shapes using a constrained nonlinear least-squares fitting protocol.

Preparation of XAS Samples. The {Fe^{2+}}PAH^T[ ] and {Fe^{2+}}-PAH^R[L-phe] samples for XAS analysis were prepared in the same way as the analogous MCD samples, except that the D_2O buffer exchanges were omitted and a final concentration of 50% glycerol was used throughout. The corresponding ferric samples were prepared in air, and no reduction step was included. The samples were loaded into Lucite EXAFS cells (23 × 1 × 3 mm) with 37 μm Kapton windows using a narrow tip pipet, capped, and frozen in the cold vapor over a pool of liquid N_2. The samples were stored at −70 °C or lower until

(48) Kappock, T. J. Ph.D. Thesis, Yale University, 1996.
(49) Siegel, L. M.; Monty, K. J. *Biochim. Biophys. Acta* **1996**, *112*, 246.
(50) Glasfeld, E.; Kappock, T. J.; Caradonna, J. P. Manuscript in preparation.
(51) Browett, W. R.; Fucaloro, A. F.; Morgan, T. V.; Stephens, P. J. *J. Am. Chem. Soc.* **1983**, *105*, 1868.

Table 2. Protein Specifications for {$Fe^{3+/2+}$}PAH XAS Samples

enzyme state	init sp act. (units mg^{-1})	protein [ ] (mg mL^{-1})	[Fe] (mM)	final sp act. (units mg^{-1})
{Fe^{3+}}PAH^{T}[ ]	7.9	191	2.8	5.0 (63%)[a]
{Fe^{2+}}PAH^{T}[ ]	7.9	150	2.2	3.4 (43%)
{Fe^{3+}}PAH^{R}[L-phe]	6.0	148	2.2	5.3 (88%)
{Fe^{2+}}PAH^{R}[L-phe]	6.0	135	2.0	4.8 (80%)

[a] Percent of initial specific activity.

analysis. Verification of the extent of reduction was performed by EPR using a Bruker ER 220D-SRC spectrometer interfaced to an IBM XT computer and a Bruker ER 042MRH microwave bridge. An Air Products LTR-3 Heli Tran continuous flow liquid helium cryostat was employed to ensure a temperature below 10 K. The samples were characterized by EPR before and after exposure to the X-ray beam to monitor damage using a sample holding unit specially adapted for use with EXAFS cells. PAH activity measurements performed on the XAS samples after spectroscopic analysis (Table 2) showed reasonably high retention of enzymatic activity, indicating little sample degradation during the time course of the measurements.

XAS Data Collection, Reduction, and Analysis. X-ray absorption spectra were recorded at the Stanford Synchrotron Radiation Laboratory (SSRL) on unfocused beamline 7-3 under operating conditions 3 GeV, 50−100 mA. The radiation was energy resolved using a Si(220) double-crystal monochromator with 1 mm high pre-monochromator beam defining slits. An Oxford Instruments continuous flow liquid helium CF1208 cryostat was used to maintain a constant sample temperature of 10 K. Energies were calibrated using an internal Fe foil standard, assigning the first inflection point to 7111.2 eV.[52] The spectrometer energy resolution was approximately 1.4 eV[53] with reproducibility in edge position determination of <0.2 eV. Data were measured to $k = 15$ Å^{-1}, detuning the monochromator 50% at 7998 eV to minimize harmonic contamination. The fluorescence signal was monitored using a 13-element Ge solid-state array detector[54] windowed on the Fe Kα signal. During the experiment, count rates of approximately 30 000 s^{-1} total per element were not exceeded. Thirty scans were collected for the {Fe^{2+}}PAH^{T}[ ] sample and 22 scans for the {Fe^{2+}}PAH^{R}[L-phe] sample. Both the {Fe^{3+}}PAH^{T}[ ] and {Fe^{3+}}-PAH^{R}[L-phe] samples photoreduced in the beam, as was evident by systematic changes in the edge shape and position. Therefore, the {Fe^{3+}}PAH^{T}[ ] sample was exposed to the beam in two different spots, and two "first" scans and a total of eleven scans were collected. Since the photoreduction of {Fe^{3+}}PAH^{R}[L-phe] was anticipated, the sample was exposed in four different spots giving four "first" scans and a total of 20 scans. The edge position of the data in the "fifth" scans was ∼1 eV lower in energy than that in the "first" scans for both ferric samples. As the total shift in the edge between the ferric and ferrous samples is ∼4 eV, if the assumption is made that there is a linear relationship between edge position and oxidation state, a ∼1 eV shift would correspond to a total fraction of 12% ferrous protein signal in the average data used in the fits, which was deemed acceptable. Furthermore, from comparison of "first" scan data to "second" scan data to "third" scan data, *etc.*, no discernible changes in the EXAFS could be detected. Therefore, the edge spectra of {Fe^{3+}}PAH^{T}[ ] and {Fe^{3+}}-PAH^{R}[L-phe] presented are averages of the "first" scans only, while the EXAFS data shown are averages of all the scans collected. A pre-edge subtraction was performed by fitting the tail of a Gaussian to the pre-edge region and subtracting this polynomial from the averaged spectra.[55] A three-segment spline approximately even in *k*-space was fitted to the EXAFS region and the data normalized to an edge jump of one at 7130 eV. The spline was chosen so that it minimized residual low-frequency background but did not reduce the EXAFS amplitude, as checked by monitoring the Fourier transform of the EXAFS during the background subtraction process.

EXAFS data reduction was performed on the normalized protein spectra according to established methods.[56−58] The normalized data were converted to *k*-space. The photoelectron wave vector, *k*, is defined by $[2m_e(E - E_0)/\hbar^2]^{1/2}$, where m_e is the electron mass, *E* is the photon energy, ħ is Planck's constant divided by 2π, and E_0 is the threshold energy of the absorption edge, which was defined to be 7130 eV for the Fe K absorption edge. EXAFS data analysis was performed with nonlinear least-squares curve-fitting techniques[52,56−58] using empirical phase and amplitude parameters. Empirical Fe−O and Fe−N backscattering parameters were obtained from $[Fe(acac)_3]$[59,60] and $[Fe(1,10\text{-phenanthroline})_3](ClO_4)_3$,[61,62] respectively. Fourier transforms (from *k*- to R-space) were performed for the data range 3.5−12.5 Å^{-1} with a Gaussian window of 0.1 Å^{-1}. The window widths used in the backtransforms (from R- to *k*-space) for the proteins are given in Results and Analysis. The window widths were kept as similar as possible to those used to extract amplitude and phase parameters from the model compounds to minimize artifacts introduced by the Fourier filtering technique. All curve-fitting was based on k^3-weighted data and applied to the individual filtered shell of interest. Only the structure-dependent parameters, the distance and coordination number, were varied unless stated otherwise. (Parallel fits where the distance and Debye−Waller factor were varied and the coordination number was fixed and systematically stepped through were also performed and gave equivalent results.) A "goodness of fit" parameter, *F*, was calculated as $F = \{[k^6(\text{data - fit})^2]/(\text{number of points})\}^{1/2}$ for each fit.

Fe K-edge spectra were also collected for four-, five-, and six-coordinate ferrous and ferric model complexes.[63] Fe(HB(3,5-*i*-$Pr_2pz)_3$)-Cl was obtained as a gift from N. Kitajima.[64] $[Fe(TMC)Cl](BF_4)$,[65] $[Fe(imidazole)_6]Cl_2$,[66] $(Et_4N)[FeCl_4]$,[67] and Fe(salen)Cl[68] were prepared as described in the literature, and $Fe(acac)_3$ was purchased from Aldrich. Fe(HB(3,5-*i*-$Pr_2pz)_3$)Cl, $[Fe(TMC)Cl](BF_4)$, and $[Fe(imidazole)_6]Cl_2$ are air-sensitive and were thus handled in a N_2-filled glovebox. Crystalline samples of the model complexes were mixed with boron nitride (BN) and ground into a fine powder. The BN/sample mixture was pressed into a 1 mm thick Al spacer that was sealed with 63.5 μm Mylar tape windows and frozen in liquid N_2. Data were measured in transmission mode with N_2-filled ionization chambers to $k = 9.5$ Å^{-1} detuning the monochromator 50% at 7474 eV to minimize harmonic contamination. Two to three scans were averaged for each sample. A smooth pre-edge background was removed from the averaged spectra by fitting a first-order polynomial to the pre-edge region and subtracting this polynomial from the entire spectrum. A two-segment spline of order 2 was fitted to the EXAFS region and the data normalized to an edge jump of one at 7130 eV. The intensities and energies of the pre-edge features were determined as described below.

The intensities and energies of pre-edge features of the model complex and protein data were quantitated with the fitting program EDG_FIT, which utilizes the double precision version of the public domain MINPAK fitting library. EDG_FIT was written by Dr. Graham N. George of the SSRL. All spectra were fitted over the range 7108−7118 eV. Pre-edge features were modeled by pseudo-Voigt line shapes (simple sums of Lorentzian and Gaussian functions).[53,69−71] A fixed 50:50 ratio of Lorentzian:Gaussian contributions for the pre-edge features successfully reproduced the spectra. Functions modeling the

(52) Scott, R. A.; Hahn, J. E.; Doniach, S.; Freeman, H. C.; Hodgson, K. O. *J. Am. Chem. Soc.* **1982**, *104*, 5364.
(53) Lytle, F. W. In *Applications of Synchrotron Radiation*; Winick, H., Xiam, D., Ye, M.-H., Huang, T., Eds.; Gordon and Breach Science Publishers: New York, 1989; p 135.
(54) Cramer, S. P.; Tench, O.; Yochum, M.; George, G. N. *Nucl. Instrum. Methods Phys. Res.* **1988**, *A266*, 586.
(55) George, G. N.; Pickering, I. J. To be published.
(56) Cramer, S. P.; Hodgson, K. O.; Stiefel, E. I.; Newton, W. E. *J. Am. Chem. Soc.* **1978**, *100*, 2748.
(57) Cramer, S. P.; Hodgson, K. O. *Prog. Inorg. Chem.* **1979**, *15*, 1.
(58) Scott, R. A. *Methods Enzymol.* **1985**, *117*, 414.
(59) Iball, J.; Morgan, C. H. *Acta Crystallogr.* **1967**, *23*, 239.
(60) Roof, R. B. J. *Acta Crystallogr.* **1956**, *9*, 781.
(61) Johansson, L. *Chem. Scr.* **1976**, *9*, 30.
(62) Johansson, L.; Molund, M.; Oskarsson, Å. *Inorg. Chim. Acta* **1978**, *31*, 117.
(63) Abbreviations used: HB(3,5-*i*-$Pr_2pz)_3$ = hydrotris(3,5-diisopropyl-1-pyrazolyl)borate; TMC = tetramethylcyclam; salen = *N*,*N*′-ethylenebis-(salicylideneiminato); acac = acetylacetonate.
(64) Kitajima, N. Private communication.
(65) Hodges, K. D.; Wollman, R. G.; Barefield, E. K.; Hendrickson, D. N. *Inorg. Chem.* **1977**, *16*, 2746.
(66) Burbridge, C. D.; Goodgame, D. M. L. *Inorg. Chim. Acta* **1970**, *4*, 231.
(67) Kistenmacher, T. J.; Stucky, G. D. *Inorg. Chem.* **1968**, *7*, 2150.
(68) Gerloch, M.; Mabbs, F. E. *J. Chem. Soc. A* **1967**, 1598.
(69) Agarwal, B. K. *X-ray Spectroscopy*; Springer-Verlag: Berlin, 1979.

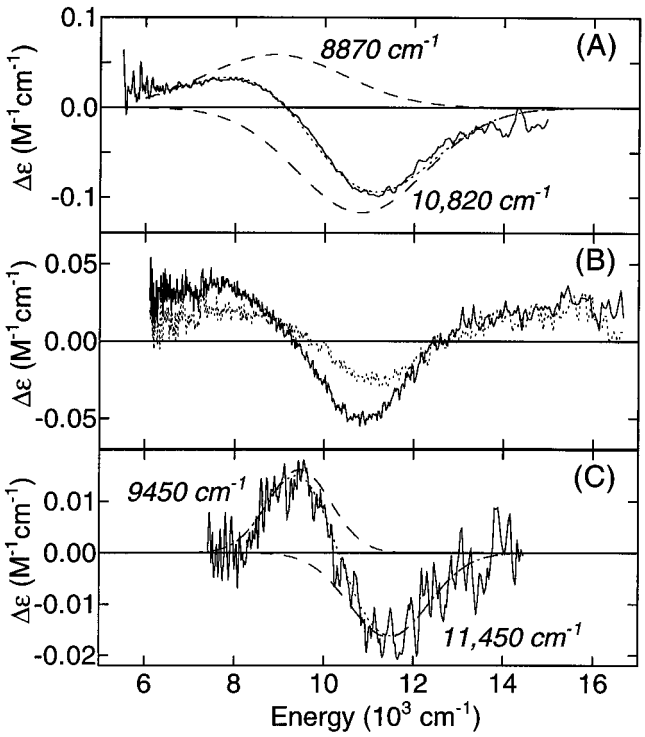

Figure 1. (A) {Fe^{2+}}PAH^T[ ] 278 K CD spectrum (—) with the Gaussian resolution showing the fit to the data (···) and individual bands (– – –). (B) Comparison of the {Fe^{2+}}PAH^T[L-trp] 278 K CD spectra in the absence (—) and presence (···) of glycerol-d_3. (C) {Fe^{2+}}PAH^R-[L-phe] 278 K CD spectrum (—) including the Gaussian resolution with the fit to the data (···) and individual bands (– – –). The energies of all of the transitions are summarized in Table 3.

background underneath the pre-edge features were chosen empirically to give the best fit and included a pseudo-Voigt function that mimicked the white line and in some cases pseudo-Voigt functions that mimicked shoulders on the rising edge. Furthermore, the second derivative of the data was compared to the second derivative of the fit and only fits where a good overall match was obtained were accepted. In all cases, a number of acceptable fits, typically eight, were obtained which equally well reproduced the data and the second derivative varying the background functions used. The value reported for the area of the fitted feature, where peak area was approximated by the height multiplied by the full-width-at-half-maximum (fwhm), is the average of all the pseudo-Voigt functions which successfully fitted the feature and its second derivative. For each sample, the standard deviation of the average of the areas was calculated to quantitate the error.

Results and Analysis

A. Circular Dichroism and Magnetic Circular Dichroism. 1. Chemical Perturbations. The 278 K CD spectrum of {Fe^{2+}}PAH^T[ ] without glycerol is shown in Figure 1A (solid line) and is identical to that of {Fe^{2+}}PAH^T[ ] in 50% glycerol-d_3 (not shown for clarity). Therefore, glycerol-d_3 may be used as a glassing agent as it does not alter the structure of the ferrous active site of PAH^T[ ]. The CD spectrum of {Fe^{2+}}PAH^T[ ] can be Gaussian resolved into two components (dashed lines in Figure 1A), a lower energy positive feature at 8870 cm^{-1} and a higher energy negative feature at 10 820 cm^{-1} with the sum of the individual Gaussians displayed as the dotted line. However, the CD spectra of {Fe^{2+}}PAH^T[L-trp] without (solid line) and with (dashed line) glycerol-d_3 displayed in Figure 1B show a shift in the band positions to lower energy (8430 and 10 540 cm^{-1}) upon addition of the substrate analog L-tryptophan, returning to similar energies (8800 and 11 000 cm^{-1}) as the resting enzyme upon addition of glycerol. Thus, the presence of L-tryptophan perturbs the iron active site, but this affect is nullified by the addition of the glassing agent, and thus low-temperature MCD is not available for the L-tryptophan-bound enzyme. This observation is consistent with EPR studies on {Fe^{3+}}PAH^T[L-trp] which suggest that glycerol displaces the substrate analog from the active site pocket.[31,33] The CD spectrum of {Fe^{2+}}PAH^R[L-phe] is shown in Figure 1C and is insensitive to addition of glycerol-d_3. The Gaussian resolution of the CD spectrum indicates transition energies of 9450 and 11 450 cm^{-1}, which are considerably higher than those of the resting enzyme. The band positions for the {Fe^{2+}}PAH CD spectra are summarized in Table 3.

Table 3. {Fe^{2+}}PAH Ligand Field Transition Energies

enzyme state	glycerol	spectrosc method	energy (cm^{-1}) band 1	band 2
{Fe^{2+}}PAH^T[ ]	no/yes	CD	8 870	10 820
{Fe^{2+}}PAH^T[L-trp]	no	CD	8 430	10 540
{Fe^{2+}}PAH^T[L-trp]	yes	CD	8 800	11 000
{Fe^{2+}}PAH^R[L-phe]	no/yes	CD	9 450	11 450
{Fe^{2+}}PAH^T[ ]	yes	MCD	8 500	10 300
{Fe^{2+}}PAH^R-NEM	yes	MCD	8 580	10 250
{Fe^{2+}}PAH^T[L-phe]	yes	MCD	9 300	10 750
{Fe^{2+}}PAH^R[L-phe]	yes	MCD	9 250	10 700

MCD was used to probe the iron centers in a variety of chemically altered {Fe^{2+}}PAH samples in order to determine which of the perturbations had an effect on the ferrous active site. The 5 K, 7 T MCD spectrum of {Fe^{2+}}PAH^T[ ] is shown as the solid line in Figure 2A. The Gaussian resolution (individual bands shown as dashed lines with sum as dotted line) reveals two positive features at 8500 and 10 300 cm^{-1}. These transitions are sharper in nature and shifted to slightly lower energy relative to their positions in the corresponding CD spectrum (Figure 1A) due to a small temperature effect on the iron site. The 5 K, 7 T MCD spectrum of {Fe^{2+}}PAH^R-NEM is shown as the solid line in Figure 2B. The spectrum can be Gaussian resolved into two component features at 8580 and 10 250 cm^{-1}. Although there is some variation in the ratio of the peak intensities relative to the resting enzyme, the transition energies are similar, suggesting that there is little change at the ferrous active site of resting {Fe^{2+}}PAH^T[ ] through nonallosteric activation with *N*-ethylmaleimide. Panels C and D of Figure 2 show the 5 K, 7 T MCD spectra of {Fe^{2+}}-PAH^T[L-phe] and {Fe^{2+}}PAH^R[L-phe], respectively, in order to decouple the effects of L-phenylalanine in the catalytic site from allosteric activation. The Gaussian resolutions for {Fe^{2+}}PAH^T-[L-phe] (Figure 2C) and {Fe^{2+}}PAH^R[L-phe] (Figure 2D) reveal two transitions at 9300 and 10 750 cm^{-1} and at 9250 and 10 700 cm^{-1}, respectively. These band positions are nearly identical to one another, indicating that there is no significant difference at the iron center of {Fe^{2+}}PAH^T[L-phe] as a result of L-phenylalanine-induced activation at the allosteric effector site, which is consistent with the similar results of activation by *N*-ethylmaleimide. Although the activation state of the enzyme has no effect on the spectral properties of the ferrous center, addition of the natural substrate L-phenylalanine to the active site pocket of {Fe^{2+}}PAH^T[ ] induces a shift of the MCD (and CD, *vide supra*) bands to higher energy, indicating a geometric change at the iron center. These perturbation studies have identified two different active site forms of PAH which are spectroscopically defined in detail below: {Fe^{2+}}PAH^T[ ] with an empty catalytic site and either {Fe^{2+}}PAH^T[L-phe] or {Fe^{2+}}-

(70) Lytle, F. W.; Greegor, R. B.; Sandstrom, D. R.; Marques, E. C.; Wong, J.; Spiro, C. L.; Huffman, G. P.; Huggins, F. E. *Nucl. Instrum. Methods Phys. Res.* **1984**, *A226*, 542.

(71) Tyson, T. A.; Roe, A. L.; Frank, P.; Hodgson, K. O.; Hedman, B. *Phys. Rev. B* **1989**, *39*, 6305.

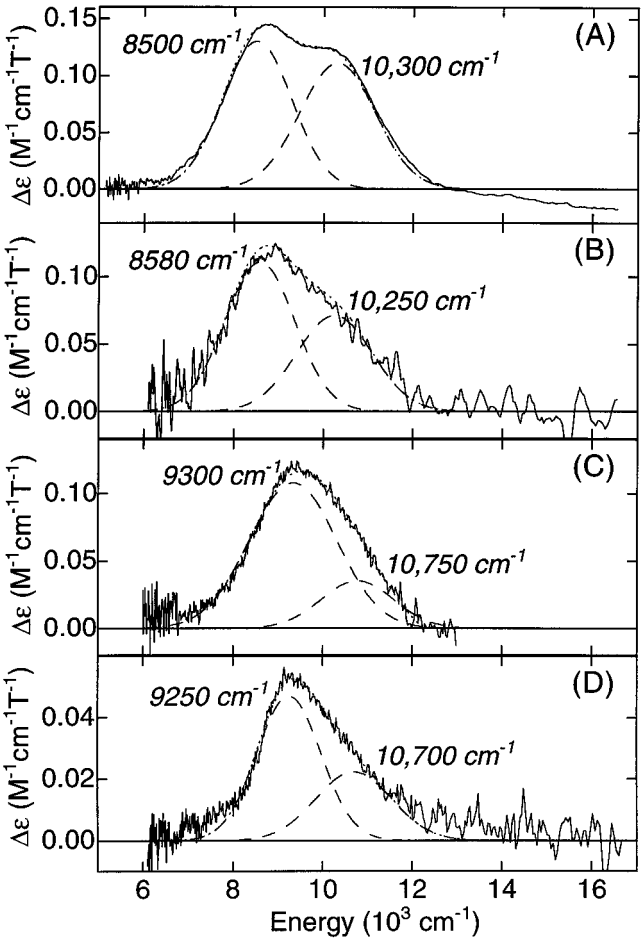

Figure 2. MCD spectra (—) at 5 K and 7 T for (A) {Fe^{2+}}PAH^T[ ], (B) {Fe^{2+}}PAH^R-NEM, (C) {Fe^{2+}}PAH^T[L-phe], and (D) {Fe^{2+}}PAH^R-[L-phe]. Each plot includes the Gaussian resolution fit to the data (···) and individual components (– – –). The energies of the transitions are summarized in Table 3.

PAH^R[L-phe] with the natural substrate L-phenylalanine bound near enough to the active site to perturb the ferrous center.

2. Spectroscopy. For a high-spin ferrous monomer with $^5T_{2g}$ ground state and ^5E_g excited state split by 10*Dq* in an octahedral field, axial and rhombic distortions will lower the symmetry of the iron site and cause the excited-state ^5E_g level to split. Two ligand field (d → d) transitions are expected corresponding to the promotion of an electron to the d_{z^2} and $d_{x^2-y^2}$ orbitals. The energy splitting between these two transitions, $\Delta^5E_g = E(d_{x^2-y^2}) - E(d_{z^2})$, can be used to obtain geometric information about the iron center.[36] A six-coordinate distorted octahedral iron center would exhibit two transitions centered around 10 000 cm^{-1} split by ~2000 cm^{-1}; a five-coordinate square pyramidal complex should have two transitions, one at an energy above 5000 cm^{-1} and a second at an energy above 10 000 cm^{-1}, with an excited-state splitting, Δ^5E_g, of ~5000 cm^{-1}; a five-coordinate trigonal bipyramidal complex would also show a large splitting between the two transitions, but the transitions would be shifted to <5000 and <10 000 cm^{-1}; a four-coordinate tetrahedral complex would have $10Dq(T_d) = (-4/9)10Dq(O_h)$ giving rise to a transition at ~5000 cm^{-1}. The 5 K, 7 T MCD spectra of {Fe^{2+}}PAH^T[ ] and {Fe^{2+}}PAH^T[L-phe] are overlaid in Figure 3. The presence of two transitions around 10 000 cm^{-1} split by ~2000 cm^{-1} is consistent with distorted octahedral coordination for both iron sites. However, the prominent shift to higher energy of the transitions in the {Fe^{2+}}PAH^T[L-phe] spectrum indicates that this iron center has a larger value of 10*Dq* (10 000 vs 9400 cm^{-1}) corresponding to a stronger ligand

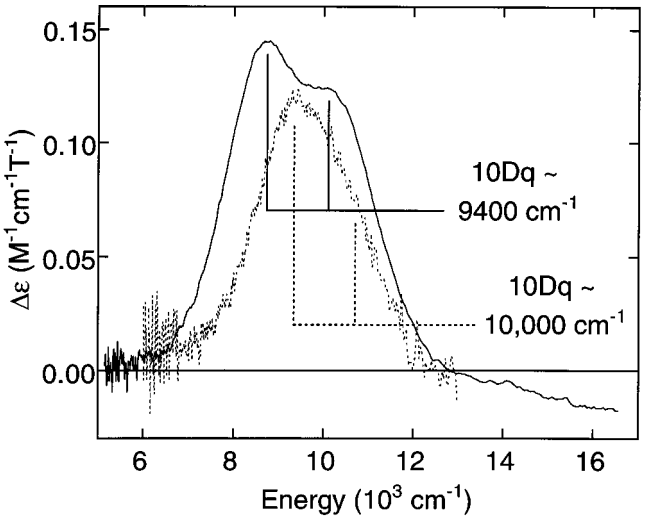

Figure 3. Comparison of the {Fe^{2+}}PAH^T[ ] (—) and {Fe^{2+}}PAH^T-[L-phe] (···) MCD spectra at 5 K and 7 T.

field at the iron center due to the presence of substrate in the active site pocket (*vide infra*).

Variable temperature variable field (VTVH) MCD was pursued on the two different active site forms of {Fe^{2+}}PAH to probe their ground-state electronic structures. The temperature dependence of the {Fe^{2+}}PAH^T[ ] MCD spectrum is shown in Figure 4A. The intensity of the MCD signal increases as the temperature is decreased. For a high-spin ferrous system with an $S = 2$ ground state this behavior can be explained for both negative ($D < 0$) and positive ($D > 0$) axial zero-field splitting (ZFS). For the more common −D situation, this temperature dependence results from *C*-term behavior[72,73] of the $M_s = \pm 2$ non-Kramers doublet electronic ground state. However, for the +D case, similar behavior results from a temperature- and field-dependent *B*-term originating from an off-axis Zeeman interaction between the $M_s = 0$ ground state and one component of the $M_s = \pm 1$ excited state dependent on the polarization and orientation of the magnetic field.[36,74] VTVH MCD saturation magnetization data can be used to distinguish the sign of *D* and are plotted for {Fe^{2+}}PAH^T[ ] in Figure 4B as a function of the reduced parameter $\beta H/2kT$ and in Figure 4C as a function of $1/kT$ in order to decouple the effects of field and temperature. The data shown were collected at 8500 cm^{-1}; however, parallel data were obtained at 10 300 cm^{-1} that show quantitatively similar behavior. The nesting, or non-superimposing, isotherms observed in the $\beta H/2kT$ plot for {Fe^{2+}}PAH^T[ ] (Figure 4B) are common to $S > {}^1/_2$ systems[75−77] and can result from either a positive or a negative ZFS.[74]

Initially to fit the data, a −D model is assumed in which the nesting behavior would result from rhombic ZFS (δ) of the $M_s = \pm 2$ non-Kramers doublet ground state.[42,43] Iteratively fitting the field, temperature, and intensity of the MCD signal as a function of δ, the splitting of the ground-state sublevels, and $g_{||}$, the magnitude of the Zeeman splitting with the applied magnetic field parallel to the *z*-axis, these spin Hamiltonian parameters can be determined. If the resulting values are out

(72) Piepho, S. B.; Schatz, P. N. *Group Theory in Spectroscopy: With Applications to Magnetic Circular Dichroism*; John Wiley & Sons: New York, 1983.
(73) Schatz, P. N.; McCafferty, A. J. *Rev. Chem. Soc.* **1967**, *23*, 552.
(74) Campochiaro, C.; Pavel, E. G.; Solomon, E. I. *Inorg. Chem.* **1995**, *34*, 4669.
(75) Johnson, M. K.; Robinson, A. E.; Thomson, A. J. In *Iron Sulfur Proteins*; Spiro, T. G., Ed.; John Wiley & Sons: New York, 1979; Vol. 4, p 367.
(76) Thomson, A. J.; Johnson, M. K. *Biochem. J.* **1980**, *191*, 411.
(77) Werth, M. T.; Johnson, M. K. *Biochemistry* **1989**, *28*, 3982.

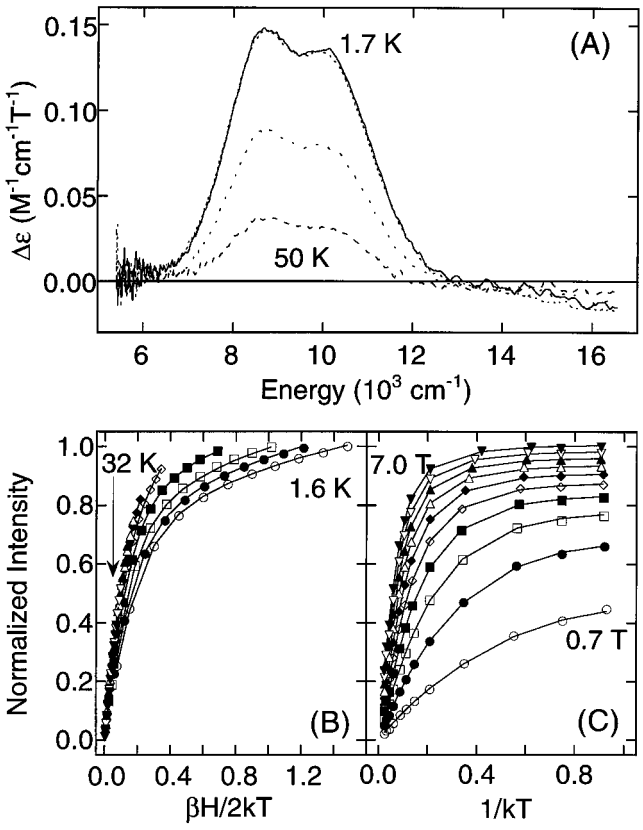

Figure 4. (A) Temperature dependence of the 7 T MCD spectra of {Fe^{2+}}PAH^T[ ] at 1.7 K (—), 5.0 K (···), 20 K (· · ·), and 50 K (- - -). (B) Variable temperature variable field saturation magnetization behavior recorded at 8500 cm^{-1}. The MCD intensity is normalized and plotted (symbols) as a function of $\beta H/2kT$ for a series of fixed temperatures (K) 1.6 (○), 1.9 (●), 2.6 (□), 4.0 (■), 7.0 (◇), 10 (◆), 13 (△), 17 (▲), 23 (▽), and 32 (▼), 45 and 60 omitted for clarity, and magnetic fields ranging from 0 to 7 T. The fit (solid lines) to the VTVH MCD data was generated from the parameters given in Table 4. (C) The normalized VTVH MCD intensity replotted (symbols) from panel B as a function of $1/kT$ for a series of fixed fields (T) 0.7 (○), 1.4 (●), 2.1 (□), 2.8 (■), 3.5 (◇), 4.2 (◆), 4.9 (△), 5.6 (▲), 6.3 (▽), and 7.0 (▼) and temperatures ranging from 1.7 to 60 K. Errors in the data points are smaller than the symbol size used.

Table 4. {Fe^{2+}}PAH Ground-State Spin Hamiltonian and Ligand Field Parameters

enzyme state	δ (cm^{-1})	$g_{\|\|}$	M_z/M_{xy}	E_S (cm^{-1})	Δ (cm^{-1})	V (cm^{-1})
{Fe^{2+}}PAH^T[ ]	3.6	9.4	−0.8	30	-500 ± 100	180 ± 50
{Fe^{2+}}PAH^T[L-phe]	4.8	6.9		11.4	900 ± 100	300 ± 60

of the range expected for a −D system, then positive ZFS must be considered. The spin Hamiltonian parameters obtained through this analysis are related to the axial and rhombic ZFS ligand field parameters Δ (the splitting of the d_{xy} and $d_{xz,yz}$ orbitals) and V (the splitting of the d_{xz} and d_{yz} orbitals) through the solution to the full $^5T_{2g}$ ligand field Hamiltonian.[36]

For {Fe^{2+}}PAH^T[ ], the best −D fit to the low temperature data where only the lowest sublevels will be populated results in $\delta = 3.6$ cm^{-1}, $g_{||} = 9.4$, and a small off-axis Zeeman contribution with a polarization ratio $M_z/M_{xy} = -0.8$. These parameters, which are within the expected range for a system with negative ZFS, are summarized in Table 4. Applying this fit to the full temperature set shows that the calculated intensities begin to vary from the experimental data points between the 32 and 45 K isotherms, suggesting that an excited state has a significant population around 25−30 cm^{-1}. Including a singlet excited state places that level at 30 cm^{-1} above the lowest

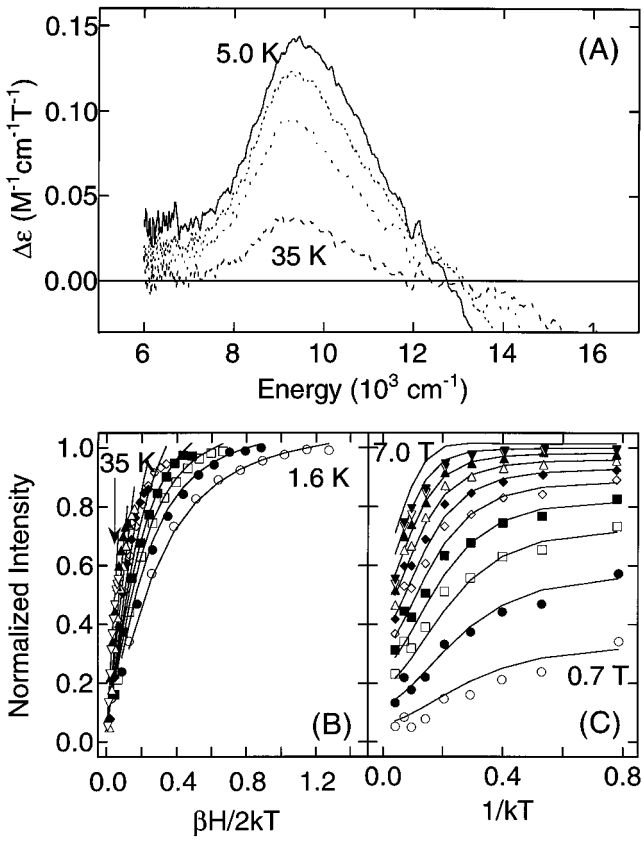

Figure 5. (A) Temperature dependence of the 7 T MCD spectra of {Fe^{2+}}PAH^T[L-phe] at 5.0 K (—), 10 K (···), 15 K (· · ·), and 35 K (− − −). (B) Variable temperature variable field saturation magnetization behavior recorded at 9100 cm^{-1}. The MCD intensity is normalized and plotted (symbols) as a function of $\beta H/2kT$ for a series of fixed temperatures (K) 1.8 (○), 2.7 (●), 3.6 (□), 4.9 (■), 7.0 (◇), 10 (◆), 15 (△), 20 (▲), and 35 (▽) and magnetic fields ranging from 0 to 7 T. The fit (solid lines) to the VTVH MCD data was generated from the parameters given in Table 4. (C) The normalized VTVH MCD intensity replotted (symbols) from panel B as a function of $1/kT$ for a series of fixed fields (T) 0.7 (○), 1.4 (●), 2.1 (□), 2.8 (■), 3.5 (◇), 4.2 (◆), 4.9 (△), 5.6 (▲), 6.3 (▽), and 7.0 (▼) and temperatures ranging from 1.8 to 35 K. Errors in the intensities are roughly twice the symbol size used.

component of the ground state. This energy is too high to be consistent with a positive value of D, in accord with the ground-state parameters. Therefore, with a negative value of D and the $M_s = \pm 2$ non-Kramers doublet lowest in energy, the $M_s = \pm 1$ doublet is $|3D|$ above the ground state and it is the lower component of this doublet which is observed at approximately 30 cm^{-1} above the ground state (Table 4). Using correlation diagrams produced from the solution to the full $^5T_{2g}$ Hamiltonian[36] to relate the ground-state spin Hamiltonian values of δ and $g_{||}$ to the axial and rhombic ZFS parameters gives $\Delta = -500 \pm 100$ cm^{-1} (the splitting of the d_{xy} and $d_{xz,yz}$ orbitals) and $V = 180 \pm 50$ cm^{-1} (the splitting of the d_{xz} and d_{yz} orbitals).

Figure 5A gives the temperature dependence of the {Fe^{2+}}-PAH^T[L-phe] MCD spectrum. The intensity of the signal decreases with increasing temperature as was also found for {Fe^{2+}}PAH^T[ ] and is indicative of C-term behavior resulting from a degenerate electronic ground state in a −D model or a non-linear B-term mechanism for the case of +D. The VTVH saturation magnetization data collected at 9100 cm^{-1} are shown for {Fe^{2+}}PAH^T[L-phe] in (Figure 5, panels B and C). The nested data were initially fitted to a −D model using only the lowest temperature data, to avoid possible contributions from populating low-lying excited states. This procedure gives $\delta =$

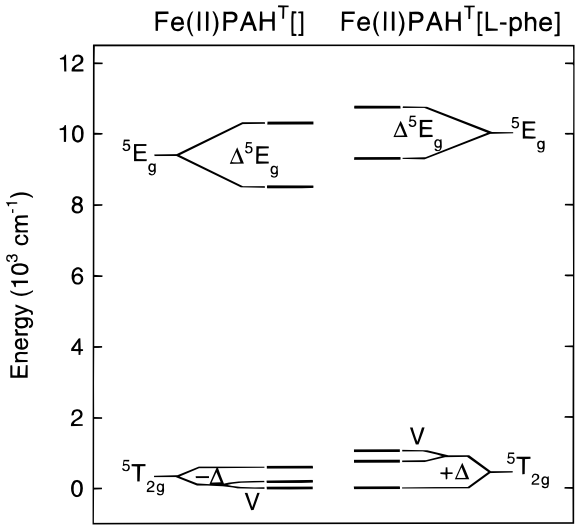

Figure 6. Experimentally determined d-orbital energy levels for $\{Fe^{2+}\}PAH^T[\ ]$ (left) and $\{Fe^{2+}\}PAH^T$[L-phe] (right).

4.8 cm^{-1} and $g_{||} = 6.9$, which is physically implausible for a −D ferrous system, where $g_{||}$ should be in the range 8.5−10.[36] Allowing for *z*-polarization does not significantly improve the value of $g_{||}$. This low value of $g_{||}$ is an indication that the ferrous site of $\{Fe^{2+}\}PAH^T$[L-phe] has a positive value of *D* and that the splitting of 4.8 cm^{-1} is the energy difference between the $M_s = 0$ ground state and the lower component of the $M_s = \pm 1$ excited state. Applying this fit to the full data set shows that the calculated intensities differ from the experimental values beginning with the 15 K isotherm, which suggests the presence of an excited state near 10 cm^{-1}. Allowing for a singlet excited state in the fit to the data places it at an energy of 11.4 cm^{-1} above the lowest sublevel as summarized in Table 4. In such a three-level model there may be Zeeman contributions to the MCD intensity for the magnetic field along both the molecular *x*- and *y*-directions,[74] which would in principle improve upon the fit (solid lines) in Figure 5 (panels B and C). The energies of the three lowest sublevels at 0, 4.8, and 11.4 cm^{-1} can be used to solve for the axial and rhombic ZFS spin Hamiltonian parameters *D* and *E*, respectively. The values obtained for $\{Fe^{2+}\}PAH^T$[L-phe] are $D = 7.6 \pm 0.2$ cm^{-1} and $E = 1.1 \pm 0.2$ cm^{-1} corresponding to a moderate degree of rhombicity with $|E/D| = 0.14 \pm 0.02$. These parameters can be related to the axial and rhombic ZFS ligand field parameters Δ and *V*, respectively, via the full $^5T_{2g}$ Hamiltonian solution,[36] and yield $\Delta = 900 \pm 100$ cm^{-1} and $V = 300 \pm 60$ cm^{-1} (Table 4), giving a total $^5T_{2g}$ splitting (Δ + *V*/2) of 1050 cm^{-1}.

From the experimental excited-state splittings and ground-state VTVH analyses, complete d-orbital energy level diagrams for the two different active site structures of $\{Fe^{2+}\}$PAH can be constructed and are presented in Figure 6. For resting $\{Fe^{2+}\}PAH^T[\ ]$ (left side of diagram) the observed ^5E_g excited state d_σ-orbital energies at 8500 and 10 300 cm^{-1} are consistent with distorted octahedral coordination for the ferrous center. The $^5T_{2g}$ ground state d_π-orbitals lie at 0, 180, and 590 cm^{-1}. These energies are as expected for six-coordinate, distorted octahedral complexes with oxygen and nitrogen ligation. For $\{Fe^{2+}\}PAH^T$[L-phe] (right side of diagram) the observed excited-state d_σ-orbital energies occur at 9300 and 10 750 cm^{-1}, which are again consistent with distorted octahedral coordination. These transition energies are shifted significantly to higher energy ($10Dq \sim 10\,000$ cm^{-1}) than those of $\{Fe^{2+}\}PAH^T[\ ]$ ($10Dq \sim 9400$ cm^{-1}). The d_π-orbitals for $\{Fe^{2+}\}PAH^T$[L-phe] also increase upon addition of substrate to lie at 0, 750, and 1050 cm^{-1} and undergo a much larger total splitting than

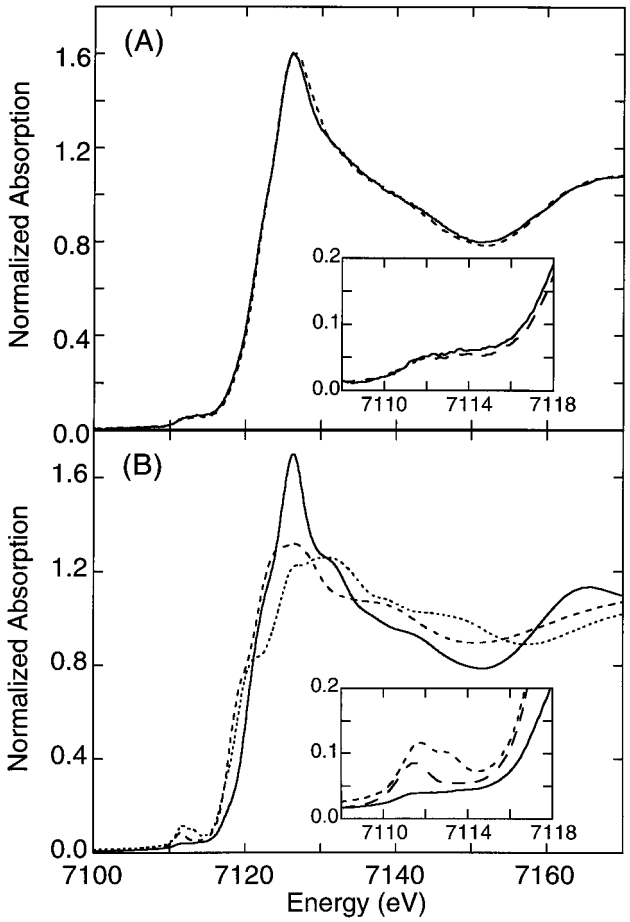

Figure 7. (A) Fe K XAS edge spectra of $\{Fe^{2+}\}PAH^T[\ ]$ (—) and $\{Fe^{2+}\}PAH^R$[L-phe] (- - -). (B) Fe K XAS edge spectra of four-, five-, and six-coordinate ferrous model complexes: Fe(HB(3,5-*i*-Pr_2pz)$_3$)Cl (···), [Fe(TMC)Cl](BF_4) (- - -), and [Fe(imidazole)$_6$]Cl_2 (—). The insets are expansions of the 1s → 3d pre-edge region.

expected by comparison to other six-coordinate, distorted octahedral ferrous complexes. These results suggest that there is a geometric change at the ferrous center of resting $PAH^T[\ ]$ induced by substrate binding to the active site pocket. This perturbation is responsible for increasing the iron ligand field strength of $\{Fe^{2+}\}PAH^T$[L-phe] compared with $\{Fe^{2+}\}$-$PAH^T[\ ]$ as well as the relative splitting of the $^5T_{2g}$ d_π-orbitals.

B. X-ray Absorption Spectroscopy. 1. Pre-Edge and Edge Analysis for $\{Fe^{2+}\}$PAH. Fe K XAS edge data of $\{Fe^{2+}\}PAH^T[\ ]$ and $\{Fe^{2+}\}PAH^R$[L-phe] have been compared to data for four-, five-, and six-coordinate ferrous model complexes to obtain information on the coordination number and the geometry of the ferrous active site of PAH. The XAS edge spectra for $\{Fe^{2+}\}PAH^T[\ ]$ and $\{Fe^{2+}\}PAH^R$[L-phe] are shown in Figure 7A while Figure 7B contains spectra of representative four-, five-, and six-coordinate ferrous model complexes: Fe(HB(3,5-*i*-Pr_2pz)$_3$)Cl,[64] [Fe(TMC)Cl](BF_4),[65] and [Fe(imidazole)$_6$]Cl_2.[66] The lowest energy peaks at ∼7112 eV arise from the weak 1s → 3d transition followed by the intense 1s → 4p transition at ∼7125 eV. This edge feature for the ferrous protein samples is very similar in shape and intensity to the six-coordinate [Fe(imidazole)$_6$]Cl_2 model, whereas it differs significantly from the edge features of the four- and five-coordinate model complexes. An expanded view of the 1s → 3d pre-edge region is shown for the proteins as well as for the model complexes as insets in Figure 7, panels A and B, respectively. The XAS spectra for $\{Fe^{2+}\}PAH^T[\ ]$ and $\{Fe^{2+}\}$-PAH^R[L-phe] both exhibit a very broad, low-intensity pre-edge which can be fitted with two features as presented in Table 5.

Table 5. XAS Pre-Edge Energies and Areas for FePAH and Model Complexes

sample[a]	oxid state	CN[b]	pre-edge energy (eV)	pre-edge area[c]	total area[c]
$\{Fe^{2+}\}PAH^{T}[\ ]$	2+		7111.72 (0.06)	4.6 (0.7)	9.9 (1.4)
			7113.58 (0.11)	5.3 (0.7)	
$\{Fe^{2+}\}PAH^{R}$[L-phe]	2+		7111.75 (0.07)	5.1 (0.7)	8.2 (1.0)
			7113.60 (0.08)	3.1 (0.7)	
$[Fe(imidazole)_6]Cl_2$	2+	6	7111.24 (0.03)	1.6 (0.5)	3.8 (0.3)
			7112.35 (0.16)	1.6 (0.8)	
			7113.66 (0.02)	0.6 (0.2)	
$[Fe(TMC)Cl](BF_4)$	2+	5	7111.41 (0.01)	10.9 (0.1)	12.9 (0.2)
			7113.43 (0.02)	2.0 (0.3)	
$Fe(HB(3,5\text{-}i\text{-}Pr_2pz)_3)Cl$	2+	4	7111.64 (0.02)	14.2 (0.5)	19.8 (0.9)
			7113.17 (0.02)	5.6 (0.9)	
$\{Fe^{3+}\}PAH^{T}[\ ]$	3+		7112.41 (0.06)	5.4 (1.4)	13.7 (4.1)
			7114.28 (0.06)	8.3 (4.5)	
$\{Fe^{3+}\}PAH^{R}$[L-phe]	3+		7112.75 (0.07)	2.3 (0.4)	8.2 (1.1)
			7114.24 (0.08)	5.9 (1.0)	
$Fe(acac)_3$	3+	6	7112.79 (0.02)	2.7 (0.3)	4.6 (0.3)
			7114.31 (0.04)	1.9 (0.1)	
Fe(salen)Cl	3+	5	7112.91 (0.01)	12.9 (0.3)	14.4 (0.6)
			7114.25 (0.07)	1.5 (0.4)	
$(Et_4N)[FeCl_4]$	3+	4	7113.16 (0.00)	20.7 (0.8)	20.7 (0.8)

[a] Abbreviations used: $HB(3,5\text{-}i\text{-}Pr_2pz)_3$ = hydrotris(3,5-diisopropyl-1-pyrazolyl)borate; TMC = tetramethylcyclam; salen = *N*,*N*′-ethylenebis(salicylideneiminato); acac = acetylacetonate. [b] CN = coordination number. [c] Pre-edge areas (errors) were determined from fits to the data, and the values reported were multiplied by 100. See the Experimental Section for a discussion of fitting procedure and error determination.

The three ferrous model complexes, $Fe(HB(3,5\text{-}i\text{-}Pr_2pz)_3)Cl$, $[Fe(TMC)Cl](BF_4)$, and $[Fe(imidazole)_6]Cl_2$, all have what appear to be two pre-edge features split by ~2 eV (*vide infra*).

The 1s → 3d pre-edge feature can be used to probe the coordination number of the iron in the active site of PAH. The 1s → 3d transition is formally electric dipole forbidden, but gains intensity through an allowed electric quadrupole transition and also by 4p mixing into the 3d orbitals when the iron atom is in a noncentrosymmetric environment. It has been shown for ferrous and ferric complexes that when the symmetry of the iron site is lowered, the pre-edge intensity increases due to an increase in the 4p−3d mixing.[78,79] A detailed multiplet analysis of the 1s → 3d pre-edge features of iron model complexes has shown that the energy splitting and intensity distribution of these features are indicative of the oxidation state, spin state, and geometry of the iron active site.[37]

When a high-spin ferrous ion is in an octahedral site, three transitions are possible for a 1s electron into $^4T_1$, $^4T_2$, and $^4T_1$ $d^{(n+1)}$ excited states. The transitions into these states are only electric quadrupole allowed as the iron atom is in a centrosymmetric environment. Thus, one observes three weak peaks in the pre-edge region, as can be seen in the $[Fe(imidazole)_6]Cl_2$ spectrum (solid line in Figure 7B inset and Table 5). In some cases, only two transitions are readily observed since the difference in energy between the lowest $^4T_1$ and the $^4T_2$ states is about the same as the energy resolution at the Fe K-edge. When a high-spin ferrous atom is in a square pyramidal site, the intensity of the lower energy pre-edge feature increases dramatically, since there is now $4p_z$ mixing into the $3d_{z^2}$ orbital due to the loss of center of symmetry, as can be seen in the $[Fe(TMC)Cl](BF_4)$ spectrum (dashed line in Figure 7B inset and Table 5). When a high-spin ferrous atom is in a tetrahedral site, there are two intense pre-edge features due to 4p mixing into the $d_{xy,xz,yz}$ orbitals, with the lower energy feature being more intense than the higher energy feature, as can be seen in the $(Fe(HB(3,5\text{-}i\text{-}Pr_2pz)_3)Cl$ spectrum (dotted line in Figure 7B inset and Table 5).

Empirically the pre-edge features of $\{Fe^{2+}\}PAH^{T}[\ ]$ and $\{Fe^{2+}\}PAH^{R}$[L-phe] (Figure 7A inset) look similar in shape and intensity to those of the six-coordinate ferrous model and quite different from those of the four- and five-coordinate complexes. The broad pre-edge features of $\{Fe^{2+}\}PAH^{T}[\ ]$ and $\{Fe^{2+}\}PAH^{R}$[L-phe] can be fitted with two peaks at energies consistent with those seen in octahedral ferrous complexes.[37] The first peak has a wider fwhm than the second peak, indicating that the first feature contains transitions into both the $^4T_1$ and the $^4T_2$ states. The first pre-edge feature of $\{Fe^{2+}\}PAH^{R}$[L-phe] is more intense than the second, as seen in an octahedral ferrous case; while in the $\{Fe^{2+}\}PAH^{T}[\ ]$ spectrum both features have approximately equal intensity. The total fitted area of the pre-edge features in the two ferrous proteins is ~9, which is higher than in the octahedral ferrous model complex and can be attributed to a less symmetric iron site caused by mixed ligation and variation in bond lengths, but less than the total area of ~13 for the five-coordinate model complex with one ligand completely removed. In general, the shapes of the main edge feature at ~7125 eV in the $\{Fe^{2+}\}PAH^{T}[\ ]$ and $\{Fe^{2+}\}PAH^{R}$[L-phe] spectra and the shapes and intensities of the corresponding pre-edge features indicate that these species have six-coordinate iron active sites with little difference between the two forms.

2. EXAFS Analysis for $\{Fe^{2+}\}PAH$. EXAFS studies of $\{Fe^{2+}\}PAH^{T}[\ ]$ and $\{Fe^{2+}\}PAH^{R}$[L-phe] were pursued to obtain metrical information on the iron active site of these different species. The EXAFS spectra are shown in Figure 8A with the Fourier transforms (FTs) calculated over the *k*-range of 3.5−12.5 $Å^{-1}$ presented in Figure 8B. Curve-fitting was performed on filtered first shell contributions over the *k*-range 4−12 $Å^{-1}$, with bond distances and coordination numbers being varied, giving the results listed in Table 6. In each case, the FT peak centered at ~1.8 Å (non-phase shift corrected) could not be adequately fitted with a single shell of either oxygen or nitrogen atoms (fits 1, 2, 7, and 8). In particular, these single-shell fits did not match the frequency of the data at higher *k* and gave unreasonably low coordination numbers. The *F* values were significantly reduced (typically by a factor of 2) when a second shell was included in the fit. The tabulated results show fits with two O waves, an O (shorter) and a N wave, an O and a N

(78) Roe, A. L.; Schneider, D. J.; Mayer, R. L.; Pyrz, J. W.; Widom, J.; Que, L., Jr. *J. Am. Chem. Soc.* **1984**, *106*, 1676.

(79) Randall, C. R.; Shu, L.; Chiou, Y.-M.; Hagen, K. S.; Ito, M.; Kitajima, N.; Lachicotte, R. J.; Zang, Y.; Que, L., Jr. *Inorg. Chem.* **1995**, *34*, 1036.

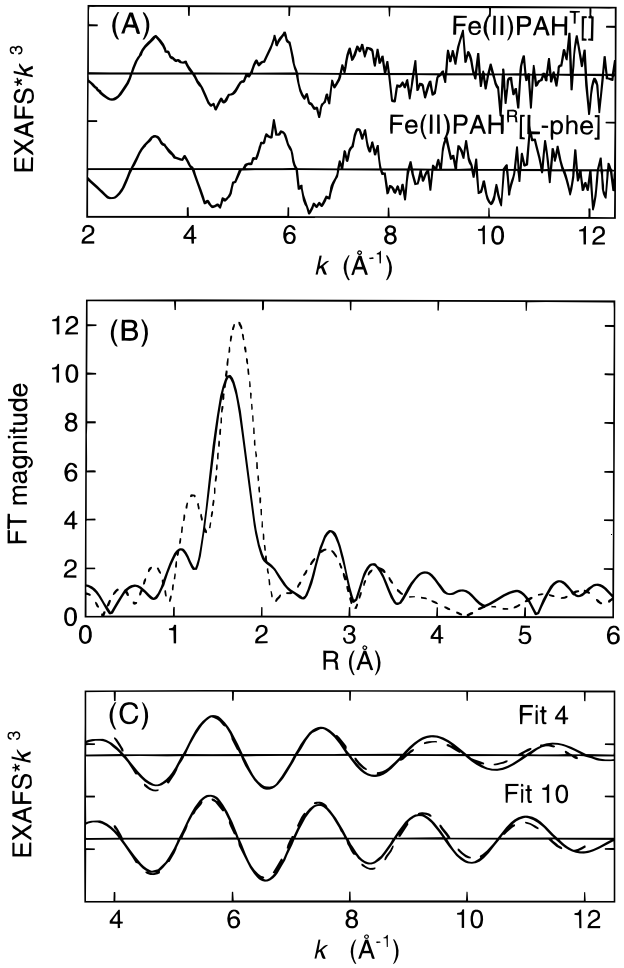

Figure 8. (A) EXAFS data (*k^3) for {Fe^{2+}}PAH^T[ ] and {Fe^{2+}}PAH^R-[L-phe] (the ordinate scale is 5 between tick marks with solid horizontal lines indicating the zero point of each plot). (B) Fourier transform (non-phase shift corrected) over the k-range 3.5−12.5 Å^{-1} of the EXAFS data of {Fe^{2+}}PAH^T[ ] (—) and {Fe^{2+}}PAH^R[L-phe] (- - -). (C) Fits (— — —) to the Fourier filtered data (—) of {Fe^{2+}}PAH^T[ ] (fit 4) and {Fe^{2+}}PAH^R[L-phe] (fit 10) (the ordinate scale is 5 between tick marks with solid horizontal lines indicating the zero point of each plot).

(shorter) wave, and two N waves. The fits are very similar in fit quality and overall results, reflecting the fact that there are only subtle differences between Fe−O and Fe−N EXAFS waves and that they can generally not be reliably distinguished in EXAFS fits. The results should therefore be interpreted as there being two shells in the first coordination sphere, made up mainly of O and O, O and N, or N and N, and EXAFS cannot reliably distinguish among these. Usually Fe−O distances are shorter than Fe−N distances, with octahedral Fe(II)−O distances at ∼2.15 Å[80−83] and Fe(II)−N distances at ∼2.20 Å.[84] The two shell fits with the O shell at a shorter distance than the N shell (fits 4 and 10) are therefore presented in comparison to the backtransformed data in Figure 8C.

There are subtle differences between the fits to the {Fe^{2+}}-PAH^T[ ] and {Fe^{2+}}PAH^R[L-phe] EXAFS data. In comparing fits 4 and 10, the total coordination number decreases from 5.9 for {Fe^{2+}}PAH^T[ ] to 4.5 for {Fe^{2+}}PAH^R[L-phe] with a marked decrease in the second shell contribution. However, the pre-edge and edge features of {Fe^{2+}}PAH^T[ ] and {Fe^{2+}}PAH^R-[L-phe] look very similar to each other and those of the six-coordinate model complex. In addition, the average distance to all the ligands in the first coordination sphere is 2.18 Å for {Fe^{2+}}PAH^T[ ] and 2.17 Å for {Fe^{2+}}PAH^R[L-phe]. These distances are typical of six-coordinate ferrous centers as crystallographic information on model complexes with oxygen and nitrogen ligation reports average bond lengths of 2.17 ± 0.03 Å for six-coordinate sites,[80−83,85−87] 2.11 ± 0.02 Å for five-coordinate sites,[88,89] and 2.00 ± 0.01 Å for four-coordinate sites.[64] This suggests that the coordination number of 4.5 extracted from the fit to the {Fe^{2+}}PAH^R[L-phe] EXAFS data is low due to correlation of the two EXAFS waves and/or static or dynamic disorder and that the ferrous active sites of {Fe^{2+}}-PAH^T[ ] and {Fe^{2+}}PAH^R[L-phe] are six-coordinate. The

Table 6. Summary of EXAFS Curve-Fitting Results

enzyme state	fit no.	FT window width (Å)	element	CN[a,b]	bond length (Å)[b]	F
{Fe^{2+}}PAH^T[ ]	1	[0.8−2.3]	N	2.9	2.14	0.91
	2	[0.8−2.3]	O	2.5	2.12	0.75
	3	[0.8−2.3]	O	3.2	2.09	0.36
			O	2.0	2.25	
	4	[0.8−2.3]	O	3.5	2.10	0.34
			N	2.4	2.29	
	5	[0.8−2.3]	O	2.5	2.22	0.27
			N	3.7	2.10	
	6	[0.8−2.3]	N	4.3	2.11	0.25
			N	3.2	2.27	
{Fe^{2+}}PAH^R[L-phe]	7	[1.0−2.15]	N	4.1	2.17	0.58
	8	[1.0−2.15]	O	3.4	2.15	0.39
	9	[1.0−2.15]	O	3.6	2.14	0.32
			O	0.7	2.29	
	10	[1.0−2.15]	O	3.7	2.14	0.32
			N	0.8	2.33	
	11	[1.0−2.15]	O	2.2	2.20	0.36
			N	2.8	2.13	
	12	[1.0−2.15]	N	4.2	2.15	0.37
			N	2.1	2.27	
{Fe^{3+}}PAH^T[ ]	13	[0.7−2.2]	N	2.8	2.08	1.1
	14	[0.7−2.2]	O	2.5	2.05	0.94
	15	[0.7−2.2]	O	1.9	1.93	0.44
			O	3.4	2.09	
	16	[0.7−2.2]	O	2.4	1.96	0.46
			N	4.0	2.14	
	17	[0.7−2.2]	O	3.7	2.08	0.44
			N	2.1	1.94	
	18	[0.7−2.2]	N	2.9	1.97	0.49
			N	4.6	2.13	
{Fe^{3+}}PAH^R[L-phe]	19	[0.9−2.15]	N	2.4	2.07	1.2
	20	[0.9−2.15]	O	2.2	2.04	0.99
	21	[0.9−2.15]	O	2.3	1.94	0.32
			O	3.2	2.10	
	22	[0.9−2.15]	O	2.7	1.96	0.33
			N	3.7	2.15	
	23	[0.9−2.15]	O	3.5	2.09	0.24
			N	2.6	1.95	
	24	[0.9−2.15]	N	3.3	1.97	0.29
			N	4.4	2.13	

[a] CN = coordination number. [b] Errors in distances (±0.02 Å) and coordination numbers (±25%) are estimated from the variance between EXAFS fitting results and values from models of crystallographically known structure.[56]

(80) Hamilton, W. C. *Acta Crystallogr.* **1962**, *15*, 353.
(81) Montgomery, H.; Chastain, R. V.; Natt, J. J.; Witkowska, A. M.; Lingafelter, E. C. *Acta Crystallogr.* **1967**, *22*, 775.
(82) Cingi, M. B.; Lanfredi, A. M. M.; Tiripicchio, A.; Cornelissen, J. P.; Haasnoot, J. G.; Reedijk, J. *Acta Crystallogr.* **1986**, *C42*, 1296.
(83) Kitajima, N.; Fukui, H.; Moro-oka, Y.; Mizutani, Y.; Kitagawa, T. *J. Am. Chem. Soc.* **1990**, *112*, 6402.
(84) Butcher, R. J.; Addison, A. W. *Inorg. Chim. Acta* **1989**, *158*, 211.
(85) Miller, L. L.; Jacobson, R. A.; Chen, Y.-S.; Kurtz, D. M., Jr. *Acta Crystallogr.* **1989**, *C45*, 527.
(86) Chiou, Y.-M.; Que, L., Jr. *J. Am. Chem. Soc.* **1992**, *114*, 7567.
(87) Zang, Y.; Elgren, T. E.; Dong, Y.; Que, L., Jr. *J. Am. Chem. Soc.* **1993**, *115*, 811.
(88) Kitajima, N.; Tamura, N.; Amagai, H.; Fukui, H.; Moro-oka, Y.; Mizutani, Y.; Kitagawa, T.; Mathur, R.; Heerwegh, K.; Reed, C. A.; Randall, C. R.; Que, L., Jr.; Tatsumi, K. *J. Am. Chem. Soc.* **1994**, *116*, 9071.
(89) Hagen, K. Private communication.

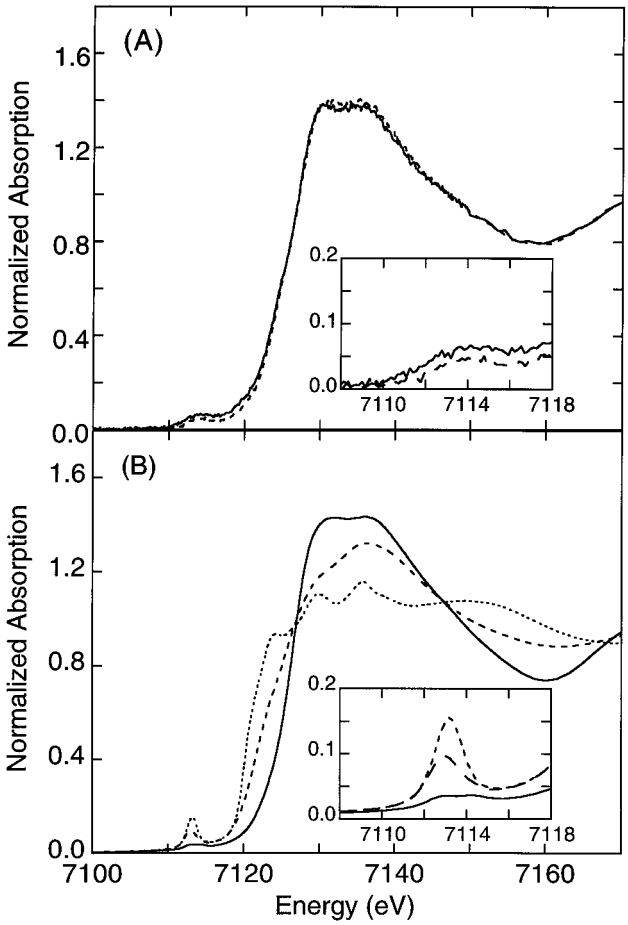

Figure 9. (A) Fe K XAS edge spectra of {Fe^{3+}}PAH^T[ ] (—) and {Fe^{3+}}PAH^R[L-phe] (- - -). (B) Fe K XAS edge spectra of four-, five-, and six-coordinate ferric model complexes: $(Et_4N)[FeCl_4]$ (•••), [Fe(salen)Cl] (- - -), and $Fe(acac)_3$ (—). The insets are expansions of the 1s → 3d pre-edge region.

distances of both the O and N shells lengthen by ∼0.04 Å in going from {Fe^{2+}}PAH^T[ ] to {Fe^{2+}}PAH^R[L-phe], but the relative contribution of the ligands at the shorter distance in all fits (except in the chemically unrealistic fits 5/11 where the long O/short N distribution has been assumed) is much greater, resulting in a lower average first coordination sphere bond length. This suggests that one active site ligand has been moved closer to the ferrous center, which is consistent with the increase in ligand field strength observed for the substrate-bound form of the enzyme in the MCD experiments.

3. Pre-Edge, Edge, and EXAFS Analysis for {Fe^{3+}}PAH. XAS edge and EXAFS analyses were also performed on {Fe^{3+}}PAH^T[ ] and {Fe^{3+}}PAH^R[L-phe] data to probe the iron site geometry and determine if phenylalanine in the active site of the ferric enzyme has the same effect as in the ferrous enzyme. XAS edge spectra for {Fe^{3+}}PAH^T[ ] and {Fe^{3+}}PAH^R[L-phe] are shown in Figure 9A, and spectra of representative four-, five-, and six-coordinate ferric model complexes, $(Et_4N)[FeCl_4]$,[67] Fe(salen)Cl,[68] and $Fe(acac)_3$,[59,60] are shown in Figure 9B. The main edge features of {Fe^{3+}}PAH^R[L-phe] and {Fe^{3+}}PAH^T[ ] look very similar to one another and the six-coordinate model complex and lie ∼4 eV to higher energy than the respective ferrous proteins (Figure 7A). However, they differ significantly in shape from the four- and five-coordinate compounds. An expanded view of the 1s → 3d pre-edge region is shown for the proteins as well as for the model complexes as insets in Figure 9, panels A and B, respectively. Spectra for {Fe^{3+}}PAH^T[ ] and {Fe^{3+}}PAH^R[L-phe] exhibit a very broad, low-intensity pre-edge which can be fitted with two features as presented in Table 5. The ferric six-coordinate complex also has two relatively weak features (4.6 total area) with an intensity ratio of 3:2. However, the five-coordinate model, Fe(salen)Cl, has two pre-edge peaks, with the lower energy peak being much more intense, and the four-coordinate complex, $(Et_4N)[FeCl_4]$, has a single intense pre-edge feature (20.7 total area).

As for the ferrous complexes, the 1s → 3d pre-edge feature can be used to probe the coordination number of the ferric active site of PAH as the intensity pattern and energy splittings are indicative of the ferric iron site symmetry.[37] When a high-spin ferric atom is in an octahedral site, two features are observed from transitions of a 1s electron into $^5T_2$ and ^5E $d^{(n+1)}$ excited states. The transitions into these states are only quadrupole allowed as the iron is in a centrosymmetric site and therefore there is no 4p−3d mixing. Thus, one observes two weak transitions with an intensity ratio of 3:2 as can be seen in the $Fe(acac)_3$ spectrum (solid line in Figure 9B inset and Table 5). When a high-spin ferric atom is in a square pyramidal site, the intensity of the lower energy transition increases dramatically, since there is now $4p_z$ mixing into the $3d_{z^2}$ orbital due to the non-centrosymmetric environment, as can be seen in the Fe(salen)Cl spectrum (dashed line in Figure 9B inset and Table 5). When a high-spin ferric atom is in a tetrahedral site, there is a single very intense pre-edge feature due to 4p mixing into the $d_{xy,xz,yz}$ orbitals, as can be seen in the $(Et_4N)[FeCl_4]$ spectrum (dotted line in Figure 9B inset and Table 5).

Empirically the pre-edge features of {Fe^{3+}}PAH^T[ ] and {Fe^{3+}}PAH^R[L-phe] (Figure 9A) are much more similar in shape and intensity to those of the six-coordinate ferric complex and quite different than those of the four- and five-coordinate models. The broad pre-edge features of {Fe^{3+}}PAH^T[ ] and {Fe^{3+}}PAH^R[L-phe] can be fitted with two peaks that are very similar in energy to the two features in the $Fe(acac)_3$ spectrum (Table 5). However, the area of the higher energy pre-edge feature in both the {Fe^{3+}}PAH^T[ ] and {Fe^{3+}}PAH^R[L-phe] data is larger than that of the lower energy feature with the total area of the fitted features being between that of the five- and six-coordinate model complexes. This could arise as the background subtraction is less accurate in protein data due to the increased noise level or because the iron site could be less symmetric due to mixed ligation and variation in bond lengths. The shapes of the main edge feature at ∼7135 eV in the {Fe^{3+}}PAH^T[ ] and {Fe^{3+}}PAH^R[L-phe] spectra and pre-edge shape and intensity together suggest that these species have six-coordinate iron centers with little difference between the sites.

EXAFS studies of {Fe^{3+}}PAH^T[ ] and {Fe^{3+}}PAH^R[L-phe] were pursued to obtain metrical information on the ferric active sites. Figure 10A contains the EXAFS spectra of {Fe^{3+}}PAH^T[ ] and {Fe^{3+}}PAH^R[L-phe] with the FTs calculated over the *k*-range of 3.5−12.5 $Å^{-1}$ shown in Figure 10B. Curve-fitting was performed on filtered first shell contributions over the *k*-range 4−12 $Å^{-1}$ with bond distances and coordination numbers being varied. Note that curve-fitting was also performed over the *k*-range of 3.8−10 $Å^{-1}$ for the {Fe^{3+}}PAH^T[ ] and {Fe^{3+}}PAH^R[L-phe] data. In addition, the averaged "first scan" data of {Fe^{3+}}PAH^T[ ] and {Fe^{3+}}PAH^R[L-phe] were fitted over the *k*-range of 3.8−10 $Å^{-1}$. The curve-fitting results over the different *k*-ranges were similar (all within the error of the technique) to those over the *k*-range of 4−12 $Å^{-1}$ that are presented in Table 6. The FT peak centered at ∼1.8 Å (non-phase shift corrected) could not be adequately fitted with a single shell of either oxygen or nitrogen atoms (fits 13, 14, 19, and 20). In particular, these single-shell fits did not match the frequency of the data at higher *k* and gave unreasonably low

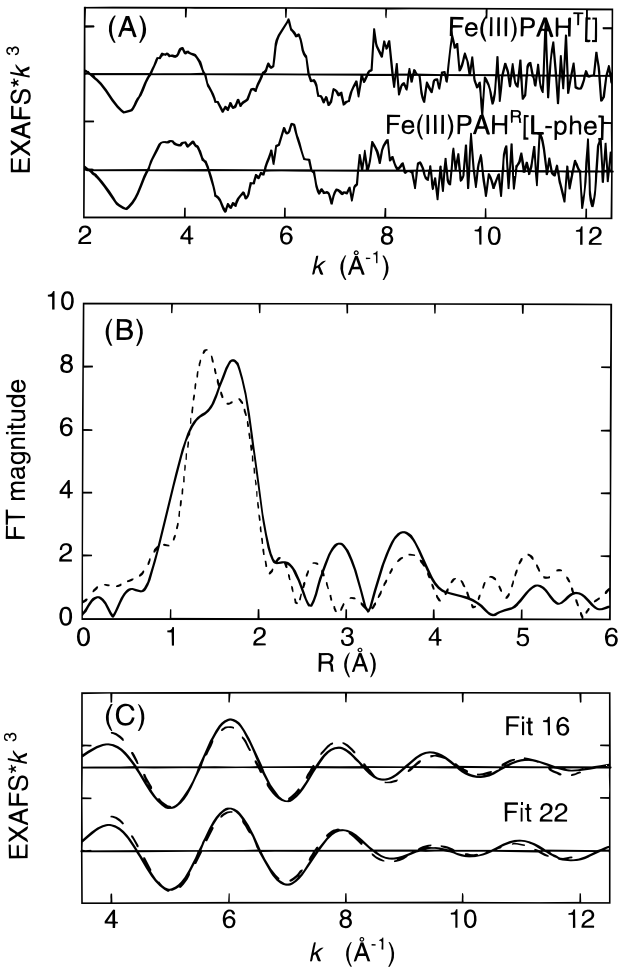

Figure 10. (A) EXAFS data (*k^3) for {Fe^{3+}}PAH^T[ ] and {Fe^{3+}}-PAH^R[L-phe] (the ordinate scale is 5 between tick marks with solid horizontal lines indicating the zero point of each plot). (B) Fourier transform (non-phase shift corrected) over the k-range 3.5−12.5 Å^{-1} of the EXAFS data of {Fe^{3+}}PAH^T[ ] (—) and {Fe^{3+}}PAH^R[L-phe] (- - -). (C) Fits (— — —) to the Fourier filtered data (—) of {Fe^{3+}}-PAH^T[ ] (fit 16) and {Fe^{3+}}PAH^R[L-phe] (fit 22) (the ordinate scale is 5 between tick marks with solid horizontal lines indicating the zero point of each plot).

coordination numbers. The F values were significantly reduced (typically by a factor of 2) when a second shell was included in the fit. The tabulated results show fits with two O waves, an O (shorter) and a N wave, an O and a N (shorter) wave, and two N waves. Usually Fe−O distances are shorter than Fe−N distances, with octahedral Fe(III)−O distances of ∼1.98 Å[90−97] and Fe(III)−N distances of ∼2.15 Å.[90−95] The two shell fits with the O shell at a shorter distance than the N shell (fits 16 and 22) are therefore presented in comparison to the backtransformed data in Figure 10C.

The fits to the {Fe^{3+}}PAH^T[ ] and {Fe^{3+}}PAH^R[L-phe] EXAFS data are extremely similar, with fits 16 and 22 having nearly identical Fe−O and Fe−N distances and similar coordination numbers. The average ligand distance is 2.07 Å in both of these fits, typical of six-coordinate ferric iron. Crystallographic information on ferric model complexes with O and N ligation reports average bond lengths of 2.03 ± 0.03 Å for six-coordinate sites,[59,60,90−97] 1.97 Å for five-coordinate sites,[98] and 1.86 ± 0.01 Å for four-coordinate sites.[99] There is a small increase in the coordination number of the shorter distance on going from {Fe^{3+}}PAH^T[ ] to {Fe^{3+}}PAH^R[L-phe]; however, this effect is not as great as that observed for the ferrous enzymes.

Discussion

There is considerably more data in the literature concerning the ferric site of PAH, yet it is the ferrous oxidation state that is the catalytically competent form of the enzyme and, thus, critical to developing an understanding of the phenylalanine hydroxylation mechanism on a molecular level. We have addressed this problem using MCD and XAS spectroscopies of a variety of {Fe^{2+}}PAH samples. From the 1800 cm^{-1} splitting in the ligand field MCD spectrum and the shape and intensity of the pre-edge features in the XAS spectrum of resting {Fe^{2+}}PAH^T[ ], the ferrous active site of PAH is six-coordinate distorted octahedral. The value obtained for 10Dq of ∼9400 cm^{-1} from the excited-state MCD spectrum is lower than those exhibited by $Fe^{II}(H_2O)_6(NH_4)_2(SO_4)_2$ (FeAS) and $Fe^{II}(H_2O)_6$-SiF_6 (FFS),[74] in which iron is surrounded by six water molecules with varying counterions. FeAS exhibits two transitions at 9200 and 10 700 cm^{-1} with 10Dq ∼ 9950 cm^{-1}, and FFS exhibits transitions at 9600 and 10 800 cm^{-1} giving 10Dq ∼ 10 200 cm^{-1}, both of which compare well with the value of 10Dq ∼ 10 000 cm^{-1} calculated empirically.[100] Carboxylate ligation is expected to reduce the ferrous ligand field strength to ∼9600 cm^{-1} while hydroxide coordination would lower it even further to ∼9400 cm^{-1}. In contrast, nitrogen ligation greatly increases the ligand field strength about an iron center as evidenced by the corresponding value of 10Dq for Fe(imidazole)$_6$Cl$_2$ of ∼11 000 cm^{-1} observed experimentally and the calculated value of ∼12 500 cm^{-1} for six NH_3 ligands. This suggests that, to account for the low ligand field strength in {Fe^{2+}}PAH^T[ ], there must be significant oxygen ligation and that the Fe−O/N first coordination sphere bond distances must be long relative to model complexes. The presence of two histidine residues at the active sites of PAH[101] and TyrH[102] has been suggested on the basis of mutagenesis studies with carboxylate oxygens and a solvent oxygen completing the coordination sphere.[91,101,103,104] The model complex Li[iron(II) methylethylenediamine triacetate](MeOH) in solution designed to mimic the proposed coordination sphere of PAH with two nitrogen ligands, three carboxylate oxygen ligands, and a solvent (oxygen) molecule exhibits MCD transitions at 9200 and 11 100 cm^{-1} with 10Dq ∼ 10 150 cm^{-1}.[38] Thus, the first coordination sphere of resting {Fe^{2+}}PAH^T[ ] must contain significant oxygen character and

(90) Ainscough, E. W.; Brodie, A. M.; Plowman, J. E.; Brown, K. L.; Addison, A. W.; Gainsford, A. R. *Inorg. Chem.* **1980**, *19*, 3655.
(91) Cox, D. D.; Que, L., Jr. *J. Am. Chem. Soc.* **1988**, *110*, 8085.
(92) Lauffer, R. B.; Heistand, R. H., II; Que, L., Jr. *Inorg. Chem.* **1983**, *22*, 50.
(93) Malfant, I.; Morgenstern-Badarau, I.; Philoche-Levisalles, M.; Lloret, F. *J. Chem. Soc., Chem. Commun.* **1990**, 1338.
(94) McDevitt, M. R.; Addison, A. W.; Sinn, E.; Thompson, L. K. *Inorg. Chem.* **1990**, *29*, 3425.
(95) Okamoto, K.-I.; Kanamori, K.; Hidaka, J. *Acta Crystallogr.* **1990**, *C46*, 1640.
(96) Raymond, K. N.; Isied, S. S.; Brown, L. D.; Fronczek, F. R.; Nibert, J. H. *J. Am. Chem. Soc.* **1976**, *98*, 1767.
(97) Clarke, E. T.; Martell, A. E.; Reibenspies, J. *Inorg. Chim. Acta* **1992**, *196*, 177.
(98) Heistand, R. H., II; Roe, A. L.; Que, L., Jr. *Inorg. Chem.* **1982**, *21*, 676.
(99) Koch, S. A.; Millar, M. *J. Am. Chem. Soc.* **1982**, *104*, 5255.
(100) Figgis, B. N. *Introduction to Ligand Fields*; Interscience Publishers: New York, 1966.
(101) Gibbs, B. S.; Wojchowski, D.; Benkovic, S. J. *J. Biol. Chem.* **1993**, *268*, 8046.
(102) Ramsey, A. J.; Daubner, S. C.; Ehrlich, J. I.; Fitzpatrick, P. F. *Protein Sci.* **1995**, *4*, 2082.
(103) Debrunner, P. G. In *EMR of Paramagnetic Molecules*; Berliner, L. J., Ruben, J., Eds.; Plenum Press: New York, 1993; Vol. 13.
(104) Martínez, A.; Andersson, K. K.; Haavik, J.; Flatmark, T. *Eur. J. Biochem.* **1991**, *198*, 675.

have longer bond distances relative to model complexes as a result of steric constraints associated with the protein ligand.

Activation from the T → R state is a critical step in the *in vivo* phenylalanine hydroxylation mechanism. Although protein structural rearrangement has been observed for this process and associated with the formation of a functional active site, until now, little has been known regarding the direct influence of activation on the ferric coordination environment, much less the catalytically relevant ferrous iron structure.[45] Comparison of the transition energies in the MCD spectra of $\{Fe^{2+}\}$-$PAH^T[\ ]$ and $\{Fe^{2+}\}PAH^R$-NEM (Figure 2, panels A and B, respectively) suggests that activation by nonphysiological methods does not affect the immediate iron binding environment. Analogously, allosteric activation by the natural substrate L-phenylalanine also does not alter the ferrous site, as evidenced by the comparable band positions in the MCD spectra of $\{Fe^{2+}\}$-PAH^T[L-phe] and $\{Fe^{2+}\}PAH^R$[L-phe] (Figure 2, panels C and D, respectively). This insensitivity demonstrated by the iron active site to both nonallosteric and allosteric methods of activation suggests that the T → R conversion (and ∼34 kcal/mol energetic barrier) appears to alter the surrounding protein backbone conformation in such a way as to reorganize the enzyme active site for its interaction with substrate, cofactor, or dioxygen, without actually perturbing the structure of the iron coordination sphere.

It has been proposed that there are actually two overlapping pterin binding sites consisting of at least a common subset of amino acid residues that are responsible for selecting the appropriate role of the reduced cofactor.[105] These studies showed that BH_4, 7,8-BH_2, 6-MPH_4, and 5-deaza-6-MPH_4 bound (1 pterin per subunit) with hyperbolic kinetics to the same site in PAH^T that is proximal to the non-heme iron site. No evidence for pterin binding to the iron center was observed. Upon activation, the pterin binding site was replaced with one characterized by a significantly decreased affinity for BH_4 and BH_2 as well as the inability to recognize the dihydroxypropyl side chain of either BH_4 or BH_2. The PAH^T → PAH^R reorganization may therefore act to reconstruct the pterin binding site, causing the pterin to bind closer to the catalytically important iron center, thereby allowing the enzyme to perform the tightly coupled hydroxylation of substrate. Additional studies showed that neither solvent accessibility nor chelator binding ability is affected by activation, suggesting that while activation affects the local environment of the iron center, it does not affect the iron site itself.[105] Thus, the activation process may be responsible for changing the location and perhaps the structure of the pterin binding domain from one that hinders catalysis (regulatory site) to one that functions during substrate turnover (catalytic site), without altering the inner coordination sphere of the iron center.[105] The spectroscopic data reported herein offer the first direct evidence that the Fe(II) site is not affected by the T → R conversion.

Although the iron active site geometry is not affected by the activation state of the enzyme, it is sensitive to the presence or absence of substrate. This is evidenced in the MCD analysis by the increases in ligand field strength and d_π-orbital splitting upon addition of L-phenylalanine, going from a −D ground state in $\{Fe^{2+}\}PAH^T[\ ]$ to a +D ground state in $\{Fe^{2+}\}PAH^T$[L-phe], as well as in the shift in the distribution of ligands from the outer shell to the inner shell within the first coordination sphere of $\{Fe^{2+}\}PAH^R$[L-phe] relative to $\{Fe^{2+}\}PAH^T[\ ]$ shown by the EXAFS analyses. A possible small shift in the same direction is seen in analyses of the $\{Fe^{3+}\}PAH^T[\ ]$ and $\{Fe^{3+}\}PAH^R$[L-phe] EXAFS. Empirical observations of active site spectral changes with addition of substrate have been made for the ferric enzyme using EPR,[31,33] ^{1}H nuclear magnetic resonance (NMR),[32] and ^{57}Fe Mössbauer spectroscopic studies.[31] The EPR spectra of $\{Fe^{3+}\}PAH^T[\ ]$ and $\{Fe^{3+}\}PAH^R$-NEM are similar to one another but different from those of $\{Fe^{3+}\}PAH^T$[L-phe] and $\{Fe^{3+}\}PAH^R$[L-phe].[31,46] Although the actual change at the iron site has not been identified, it is clearly the result of substrate interacting near the active site pocket. It has been suggested on the basis of ^{1}H-NMR studies[32] that a labile water molecule is displaced upon substrate binding, leading to a five-coordinate intermediate. However, our MCD results on the ferrous enzyme rule out a substrate-induced five-coordinate species, and direct coordination by L-phenylalanine to re-form a six-coordinate site is not expected. In fact, NMR studies performed on Co(II)-substituted TyrH show that the aromatic ring of phenylalanine, which can serve as a substrate for hydroxylation by this enzyme, is in the "second coordination sphere" of the metal ion, but that neither the amino nor carboxyl groups are near enough to be directly bound to the iron.[106] Therefore, substrate binding causes either a substitution of one endogenous ligand for another or, more likely, a rearrangement of the existing active site ligands, resulting in a stronger iron ligand field strength in $\{Fe^{2+}\}PAH^T$-[L-phe] relative to $\{Fe^{2+}\}PAH^T[\ ]$, without altering the nature of those ligands.

At concentrations of L-phenylalanine required for allosteric activation, substrate will also be present at the catalytic site and induce this structural rearrangement of the active site ligands prior to reaction with pterin and dioxygen, according to the sequential mechanistic order. Biopterin binding to the ferrous site prior to substrate activation will result in competitive inhibition of the enzyme and prevention of substrate activation.[1] Furthermore, the binding of L-phenylalanine to PAH^R is noncompetitive with respect to BH_2 and 5-deaza-6-MPH_4, implying that the hydroxylation reaction proceeds through a single enzyme−substrate complex.[1] With unnatural substrates, which bind with decreased affinity, the hydroxylation reaction can be partially or completely uncoupled, suggesting that there is a steric component to achieving coupled catalysis. This is evidenced in the CD spectra of $\{Fe^{2+}\}PAH^T[\ ]$, $\{Fe^{2+}\}PAH^T$-[L-trp], and $\{Fe^{2+}\}PAH^R$[L-phe] (Figure 1, panels A−C, respectively), which show that the presence of the unnatural substrate L-tryptophan causes a reversible perturbation at the iron active site that is different from the change at the ferrous center caused by the natural substrate L-phenylalanine. The presence of the natural substrate L-phenylalanine is believed[31,46] to reduce the microheterogeneity at the iron site in preparation for reaction with dioxygen and catalysis.

The kinetic studies by Shiman *et al.* also suggest that the activation-dependent structural change in PAH involves reorganization of the substrate binding site.[105] The lack of any observed influence on the binding of iron chelators or solvent accessibility suggested that activation of PAH induced a reorganization of the protein near the iron center but not the immediate environment of the iron center. However, while the MCD studies described above clearly show the iron environment to change upon substrate binding, this new environment is independent of the state of activation of the enzyme with both PAH^T[L-phe] and PAH^R[L-phe] states showing equivalent spectral features. These observations suggest that either PAH^T[L-phe] and PAH^R[L-phe] have the same substrate binding site or the iron center is relatively insensitive to any differences originating from L-phenylalanine binding to the two putative sites.

(105) Shiman, R.; Xia, T.; Hill, M. A.; Cray, D. W. *J. Biol. Chem.* **1994**, *269*, 24647.

(106) Martínez, A.; Abeygunawardana, C.; Haavik, J.; Flatmark, T.; Mildvan, A. S. *Biochemistry* **1993**, *32*, 6381.

Similar dependence on mechanistic order has been observed for other mononuclear non-heme ferrous systems. Substrate addition to Fe(II) soybean lipoxygenase-1, which catalyzes hydroperoxidation,[6] converts a five- and six-coordinate mixture to a pure six-coordinate form.[40] Resting phthalate dioxygenase is six-coordinate and binds substrate for *cis*-dihydroxylation[9] to form a mixture of square pyramidal and trigonal bipyramidal five-coordinate species, the former of which has an open axial coordination site for small molecule or dioxygen binding.[41] Catechol 2,3-dioxygenase[7] has a five-coordinate ferrous center for which substrate addition perturbs and activates the site for small molecule binding and dioxygen reaction.[42] Thus, there is precedence for substrate-induced activity enhancement at mononuclear non-heme ferrous active sites, which is clearly distinct from the substrate-induced activation at the allosteric effector site also required in the PAH mechanism.

In summary, a combination of MCD and XAS spectroscopies has been employed to effectively probe for the first time the resting catalytically active ferrous site of PAH. $\{Fe^{2+}\}PAH^{T}$-[ ] is six-coordinate, distorted octahedral with slightly longer bond distances than observed for Fe−O/N ligation in small molecule complexes. Conversion from the PAH^{T} to PAH^{R} state via allosteric as well as nonallosteric methods does not affect the catalytic iron site and thus appears to regulate the protein conformation, perhaps causing a change in the location of the pterin binding domain relative to the iron active site. However, substrate addition, with or without activation, significantly increases the ligand field strength at the ferrous active site due to an increased contribution from the ligands in the inner subshell of the first coordination sphere. From correlations to mechanistic studies this structural rearrangement of the iron active site is required prior to cofactor and dioxygen binding and leads to coupled turnover. MCD and XAS experiments are currently being extended to probe the interaction of the substrate-free and substrate-bound forms of the ferrous active site of PAH with cofactors and small molecule analogs of dioxygen to determine how geometric differences relate to the electronic structure of PAH and ultimately to its reactivity.

Acknowledgment. This work was supported by grants from the National Institutes of Health (GM40392, E.I.S.), National Science Foundation (CHE-9423181, K.O.H.), American Chemical Society (25963AC, J.P.C.), and the Camille and Henry Dreyfus and Alfred P. Sloan Foundations (J.P.C.). The SSRL is supported by the U.S. Department of Energy, Office of Basic Energy Science, Divisions of Chemical and Materials Sciences, and in part by the National Institutes of Health, National Center for Research Resources, Biomedical Research Technology Program (RR-01209, K.O.H.), and the U.S. Department of Energy, Office of Health and Environmental Research. T.J.K. thanks the Howard Hughes Medical Institute for a predoctoral fellowship.

JA962269H